BAMS Article

The Radiative Effect on Cloud Microphysics from the Arctic to the Tropics

Xiping Zeng, Andrew J. Heymsfield, Zbigniew Ulanowski, Ryan R. Neely III, Xiaowen Li, Jie Gong, and Dong L. Wu

ABSTRACT: Cloud representation is one of the largest uncertainties in the current weather and climate models. In this article, the observations and modeling of the radiative effect on (cloud) microphysics (REM) from the Arctic to the tropics are overviewed, providing a new direction to meet the challenge of cloud representation. REM deals with the radiation-induced temperature difference between cloud particles and air. It leads to two common phenomena observed at the surface—dew and frost—and impacts clouds aloft significantly, which is noticed via the wide occurrence of horizontally oriented ice crystals (HOICs). However, REM has been overlooked by all of the operational weather and climate models. Based on the bin model of REM and the global distribution of radiative cooling/warming, the observations of REM from several platforms (e.g., aircrafts, field campaigns, and satellites) are coordinated in this article, yielding a global picture on REM. As a result, the picture is compatible with the global distribution of HOICs and other ice crystal characteristics obtained from various clouds on the globe, such as diamond dust (or clear-sky precipitation) in the Arctic, subvisual cirrus clouds in the tropical tropopause layer, and other cirrus clouds from the low to high latitudes. In addition, ice crystals possess relatively strong REM compared to liquid drops because their aspect ratio is usually not one. The global picture on REM can be used by the weather and climate modelers to diagnose their cloud representation biases. It can also be used to improve the atmospheric ice retrieval algorithm from satellite observations.

KEYWORDS: Arctic; Clouds; Drizzle; Ice crystals; Radiative transfer; Cloud parameterizations

https://doi.org/10.1175/BAMS-D-21-0039.1

Corresponding author: Dr. Xiping Zeng, xiping.zeng.civ@army.mil

Supplemental material: https://doi.org/10.1175/BAMS-D-21-0039.2

In final form 3 February 2022

AFFILIATIONS: Zeng—Army Research Laboratory, Adelphi, Maryland; **Heymsfield**—National Center for Atmospheric Research, Boulder, Colorado; **Ulanowski**—British Antarctic Survey, Cambridge, and University of Manchester, Manchester, United Kingdom; **Neely**—National Centre for Atmospheric Science, University of Leeds, Leeds, United Kingdom; **Li**—NASA Goddard Space Flight Center, Greenbelt, and Morgan State University, Baltimore, Maryland; **Gong***—NASA Goddard Space Flight Center, Greenbelt, and Universities Space Research Association, Columbia, Maryland; **Wu**—NASA Goddard Space Flight Center, Greenbelt, Maryland
* CURRENT AFFILIATION: University of Maryland Baltimore County, Baltimore, Maryland

Clouds change climate by modulating the radiative equilibrium of the Earth (Liou 1986; Stephens et al. 1990; Zeng et al. 2009; Heymsfield et al. 2017). They also change weather by modulating atmospheric stability and thus large-scale vertical circulations (Slingo and Slingo 1988, 1991; Raymond 2000; Raymond and Zeng 2000). Hence, clouds work as a key part in both the water and energy cycles of the atmosphere.

The current atmospheric models, however, do not represent clouds well. The global models have the biases of "excessive water vapor" and "too dense clouds" (Zhang et al. 2001; Nam et al. 2012; Jiang et al. 2012, 2015). The high-resolution models have similar biases even in different regions, such as the Arctic (Klein et al. 2009; Morrison et al. 2011), the midlatitudes (Zeng et al. 2007), and the tropics (Powell et al. 2012; Zeng et al. 2013; Franklin et al. 2016). All of the models perform imperfectly in cloud representation, because they overlook some cloud processes, such as the radiative effect on (cloud) microphysics (REM).

REM leads to two daily phenomena in unsaturated air: dew and frost. When radiation cools the ground surface, water vapor condenses/deposits on the ground surface even though the air is still unsaturated. Cloud particles near cloud top, just as dew/frost forms, can grow at the expense of water vapor, suggesting REM is a candidate to mitigate the bias of excessive water vapor.

REM has been studied for about six decades. Fuchs (1959) first introduced a radiative term into the diffusional drop growth equation by treating the atmosphere as a blackbody, and then concluded that REM is negligible except for large drops. In fact, the atmosphere is quasi-transparent for infrared radiation (IR) with wavelengths of 8–12 μm. Hence, REM is important in thin clouds or near the edge of thick clouds, which motivated the later studies (Heymsfield 1973; Roach 1976; Hall and Pruppacher 1976; Stephens 1983; Wu et al. 2000; Lebo et al. 2008; Zeng 2008, 2018a,b; Brewster et al. 2020).

REM was previously neglected partly because it is complicated for radiation transfer and ice crystal habit and orientation. Mathematically, it is a process in a geometric space with 10 dimensions (i.e., 4 for space and time; 2 for radiation direction; 1 for radiation wavelength; and 3 for ice crystal size, shape, and orientation), and thus its simulations usually need high-performance computing. Physically, REM entangles macroscale variables of radiation transfer in the atmosphere with microscale variables of individual ice crystals. Moreover, the REM process is nonlocal: an ice crystal in the tropical tropopause layer, for example, can receive IR emitted by the clouds far below and/or by the ground surface. Hence, it is a challenge to represent REM in the weather and climate models with limited computational resources.

To simplify REM, the radiative ratio of η_z was introduced to separate the macroscale and microscale variables in REM (Zeng 2008, 2018a) [see Eq. (5) for its definition]. The ratio was used to classify REM (see section "Three modes of REM"), suggesting that REM be split into

three subtopics: 1) microscale study of individual ice crystals and ice crystal spectrum with a given η_z (Fuchs 1959; Heymsfield 1973), 2) macroscale study for the spatial and temporal variations of η_z (Stephens 1983; Harrington et al. 2000; Zeng 2008; Klinger et al. 2019), and 3) the interaction between the microscale and macroscale processes (or the interaction between η_z and clouds; Bott et al. 1990). In reference to the three subtopics, the major studies over the past decades are reviewed in Tables 1 and 2 for ice and warm clouds, respectively, with their clouds studied, methodology used, and conclusions obtained.

With the bin model of REM becoming mature (Zeng 2018a) and new observations available (Neely et al. 2013; Goerke et al. 2017; Zeng et al. 2019), REM is evaluated with specific observations (Zeng et al. 2021). In this article, the prediction of REM is compared to the ice crystal observations from the Arctic to the tropics, beginning with the physics of frost formation and REM.

Physics of frost formation

Frost (or water vapor deposition) forms on particles because radiative cooling decreases particle temperature. Consider a spherical particle aloft with radius r and temperature T_s. It is immersed in an air parcel with temperature T and relative humidity H_i with respect to ice. Its critical relative humidity is defined as

$$H_{ic} = E_{si}\left(T_s\right)\Big/E_{si}\left(T\right), \tag{1}$$

where $E_{si}(T)$ denotes the saturation vapor pressure over ice at temperature T. When $H_{ic} < H_i$, water vapor diffuses inwards and then deposits on it, bringing about frost. Otherwise, it has no frost and sublimates if it is composed of ice.

Radiation changes T_s, bringing about $T_s \neq T$ and thus $H_{ic} \neq 1$. Consider the particle at its critical case of $H_{ic} = H_i$. It exchanges energy with its environment via two processes: conduction and radiation. It receives conductive energy from its environment with a rate (Mason 1971)

$$Q_c \propto 4\pi r\left(T - T_s\right). \tag{2}$$

Meanwhile, it emits and absorbs IR, losing energy with a rate (Zeng 2008)

$$Q_r \propto 4\pi r^2\left(1-\eta\right), \tag{3}$$

where η denotes the ratio of infrared flux incident on particle surface to the radiative flux emitted by the same particle at ambient temperature T.

At the critical case, the two rates reach a balance or $Q_r = Q_c$. Substituting Eqs. (2) and (3) into $Q_r = Q_c$ yields

$$T_s - T \propto r\left(\eta - 1\right), \tag{4}$$

which shows that $T_s - T$, the particle–air temperature difference, is directly proportional to r. A similar expression for a nonspherical particle was derived, which still holds a positive correlation between $T_s - T$ and particle size (or equivalent radius r)[1] (Zeng 2008).

Equation (4) also shows that $T_s - T$ is proportional to $\eta - 1$. Since η varies with particle shape and orientation, another radiative ratio

$$\eta_z = \frac{F^+ + F^-}{2\sigma T^4} \tag{5}$$

[1] The equivalent radius of a nonspherical particle is defined as $r = S/(4\pi C)$, where S and C denote the surface area and stationary diffusion shape factor of the particle, respectively. Since it degenerates into radius for a spherical particle, it is used to measure ice particle size as well.

Table 1. Models and observations of REM for ice particles.

Publication	Cloud	Characteristics	Conclusion/implication
		Models	
Heymsfield (1973)	Individual ice crystals Ice cloud top	Ice crystals lose energy to space by radiation	Radiative cooling enhances the growth of ice crystals near cloud top
Hall and Pruppacher (1976)	Individual ice crystals Unsaturated air	Theoretical representation of REM	Radiation suppresses the sublimation of ice crystals in unsaturated air
Stephens (1983)	Individual ice crystals	Proper treatment of radiation	Radiative cooling (warming) enhances (suppresses) crystal growth (sublimation)
		Introduction of solar radiation	The larger a crystal, the stronger its REM
Wu et al. (2000)	Multiple ice crystals Bin model	Modeling of the radiative effect on ice crystal spectrum	Exhibiting a warming case where large crystals sublimate while small ones grow by deposition
Zeng (2008)	Multiple ice crystals Bin model	Analytical expression of REM $\eta_z - 1$ is used to separate radiative cooling and warming	An air parcel with $\eta_z < 1$ is colloidally unstable Radiative cooling (or $\eta_z < 1$) can bring about precipitating crystals at the expense of small crystals
	Subvisual cirrus clouds		Subvisual cirrus clouds are related to clouds below via REM
Zeng (2018a)	Bin model Diamond dust	Introduction of ice crystal orientation	Radiative cooling favors the formation of HOICs Diamond dust can form in subsaturated air via REM
		Observations	
Braham and Spyers-Duran (1967)	Survival of ice crystals in a dry environment Midlatitude	Aircraft observations revealed that ice crystals can survive a fall of kilometers through dry air	Questioning the classic equation for ice crystal growth without REM Supporting Mode I of REM
Heymsfield (1986)	Subvisual cirrus clouds TTL	Aircraft observations discovered subvisual cirrus clouds	Presenting a similarity between subvisual clouds and arctic clouds
Winker and Trepte (1998); Schwartz and Mace (2010)	Subvisual cirrus clouds Globe	Spaceborne lidars revealed that subvisual cirrus is separated from, but tends to occur with, the cirrus below	Radiation can connect subvisual cirrus to the cirrus below via REM
Noel and Chepfer (2010); Kikuchi et al. (2021)	Thin cirrus clouds	*CALIPSO* revealed that HOICs are rare, with ~6% of all ice cloud layers	HOICs occur below 10 km altitude (or cloud temperature above −30°C), whereas few above 10 km
	Globe		Frequency of clouds with HOICs increases with latitude
Neely et al. (2013)	Cirrus clouds Arctic	CAPABL was developed to measure diattenuation or HOICs	Observations revealed there are more HOICs in the upper portion of cirrus clouds than in the lower one
Goerke et al. (2017)	Cirrus clouds Arctic	2D reflections of lidar beam revealed that small ice crystals sublimates while large ones grow by deposition	Supporting Mode II of REM
Gong et al. (2018)	Thick cirrus clouds Tropics	GMI 166PD revealed a strong diurnal oscillation of 166PD over land but a weak one over oceans	Suggesting that the solar radiation cannot lead to the diurnal variation of GMI 166PD directly
Zeng et al. (2019)	Thick cirrus clouds Globe	GMI 166PD revealed the global distribution of HOICs	HOICs in thick clouds are common from the low to high latitudes
Padullés et al. (2021)	All clouds Globe	Polarimetric Radio Occultation (PRO) observations revealed the vertical variation of HOICs	The contribution of HOICs to PRO decreases with altitude
Zeng et al. (2021)	Thick cirrus clouds Globe	GMI 166PD revealed HOICs vs cloud top altitude	GMI 166PD decreases with cloud altitude Supporting that the time scale of REM increases with cloud altitude

Table 2. Models and observations of REM for liquid drops.

Publication	Cloud	Characteristics	Conclusion
		Models	
Fuchs (1959)	Individual drops	Assuming the drops and ambient air are blackbodies	REM is negligible for small droplets
Roach (1976)	Warm fog	The atmosphere is quasi transparent at the atmospheric windows	Influence of radiation on droplet growth is significant in fog
	Multiple drops	Modeling of droplet spectrum	
Bott et al. (1990)	One-dimensional fog model	Interaction between REM and gravitational drop settling	REM impacts the life cycle of fog significantly The interaction explains the observed oscillations of liquid water content and radiative flux
Austin et al. (1995)	One-dimensional stratocumulus model	Rain initiation	REM near cloud top can accelerate rain initiation
Harrington et al. (2000)	Two-dimensional stratus model	The production of drizzle-sized drops	The formation of drizzle-sized drops depends on the residence time of air parcel near cloud top
Hartman and Harrington (2005a,b)	Large-eddy model with bin physics	Solar radiation	Solar radiation warming partially offsets the IR radiative cooling near cloud top
Zeng (2018b)	Bin model	Quantifying REM in rain initiation given η_z	REM can initiate rain in any regions with $\eta_z < 1$ (e.g., very thin warm clouds in the lower troposphere)
		Observations	
Small and Chuang (2008)	Field observation of drop spectrum	Observing with the phase Doppler interferometer	Drop spectrum is broader near cloud top than below
Brewster et al. (2020)	Droplet mist in an experimental apparatus	Laboratory experiment Artificially controlling the radiative cooling	Replicating the drop spectrum broadening induced by radiative cooling

is introduced that is independent of particles, where σ is the Stefan–Boltzmann constant, and F^+ and F^- are the upward and downward IR fluxes in the atmosphere with positive magnitudes, respectively (Zeng 2008, 2018a). Clearly, η_z varies from one air parcel to another but does not change with particles inside. It determines η of a particle inside as (Zeng 2018a)

$$(\eta - 1) = \alpha(\eta_z - 1), \tag{6}$$

where $0 \le \alpha \le 1$, and α depends on particle size, shape, and orientation [see Eqs. (13)–(17) of Zeng (2018a) for the expression of α]. In general, the particle with horizontal orientation possesses larger α than the same particle with vertical orientation.

Substituting Eq. (6) into Eq. (4) yields[2]

$$T_s - T \propto \alpha r(\eta_z - 1), \tag{7}$$

which exhibits particle temperature T_s versus particle size, shape, and orientation for a given η_z. When $\eta_z < 1$ (radiative cooling), the larger the particle, the lower its T_s (or H_{ic}) is, which explains the daily phenomenon: frost forms more frequently on wide grass leaves than on narrow ones. Moreover, a horizontally oriented particle possesses lower T_s (or H_{ic}) than a vertically oriented one when $\eta_z < 1$, which explains the phenomenon that frost forms more frequently on car front windows than on side windows, for the former loses energy to space more efficiently than the latter.

[2] Once an ice particle deviates from the critical case, it sublimates or water vapor deposits on its surface, producing latent heating. After incorporating the latent heating, Eq. (7) becomes complicated while it still contains the factor of $\alpha r(\eta_z - 1)$. A complete equation of $T_s - T$ with latent heating was presented in Zeng (2008).

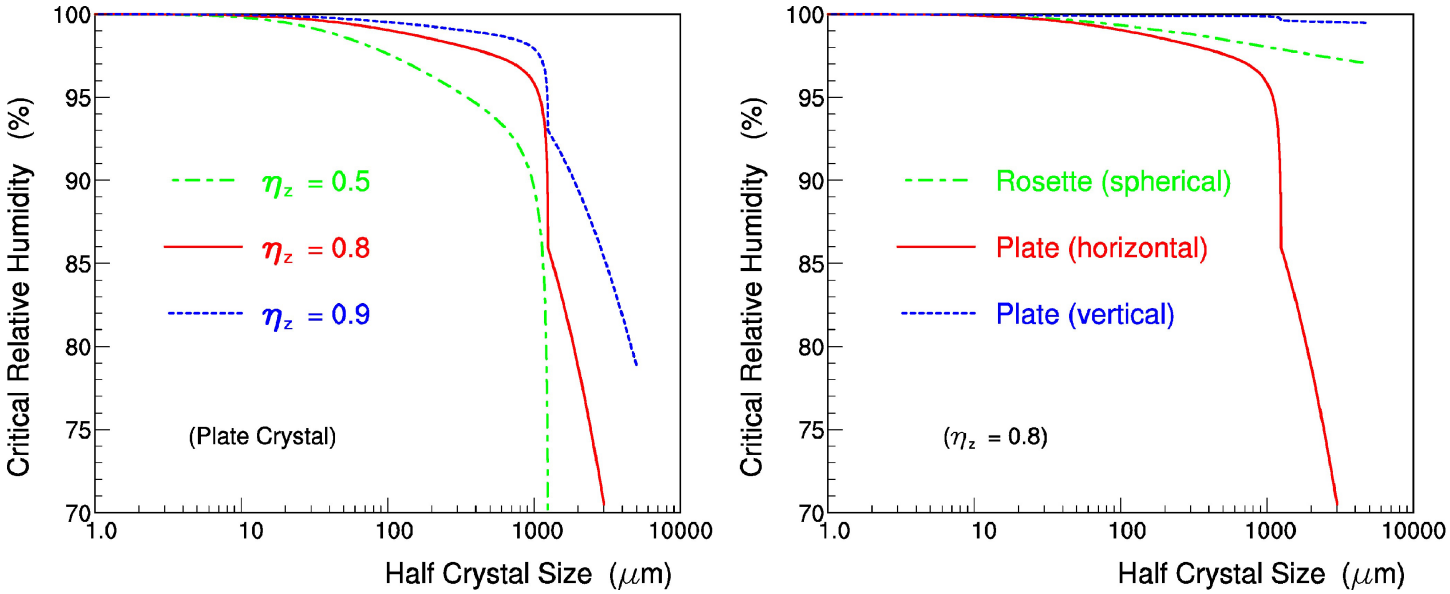

Fig. 1. Critical relative humidity H_{ic} vs half crystal size (or semi-major axis length) at T = −30°C and p = 680 hPa for (left) horizontally oriented plate-like crystals with different η_z and (right) ice crystals with different shape and orientation at η_z = 0.8.

Three modes of REM

The analytic expression of H_{ic} is derived via T_s (Zeng 2008, 2018a). It is computed with the observed ice crystal shape, mass, terminal velocity, and dimensional relationship (Auer and Veal 1970; Heymsfield 1972; Heymsfield and Iaquinta 2000). Figure 1 displays H_{ic} versus ice crystal size, shape, and orientation as well as η_z. To be specific, H_{ic} increases with η_z; H_{ic} of a horizontally oriented ice crystal (HOIC) is lower than that of a vertically oriented one; and H_{ic} of a plate-like HOIC at η_z = 0.8 starts its dramatic decrease against crystal size at half crystal size of ~500 μm, which is attributed to the dendritic extensions at crystal size $>$ 200 μm.

Consider multiple ice particles in an air parcel with relative humidity H_i. Since their H_{ic} varies with crystal size, shape, and orientation, some of them with $H_{ic} > H_i$ shrink via sublimation, whereas the others with $H_{ic} < H_i$ grow via deposition. As a result, radiation alters the particle size distribution, which is referred to as REM.

REM is classified into two types: radiative cooling and warming, which are represented by η_z <1 and >1, respectively, because $H_{ic} - 1 \propto T_s - T \propto \eta_z - 1$. The two types of REM function oppositely in the evolution of ice crystal spectrum, which is discussed below in turn.

REM with radiative cooling. An air parcel with $\eta_z < 1$ is colloidally unstable (Zeng 2008), which exhibits as three modes:

- Mode I deals with the water transfer between water vapor and ice crystals, where radiative cooling enhances (or slows) ice crystal deposition (or sublimation) (Heymsfield 1973; Hall and Pruppacher 1976; Stephens 1983). The mode causes the dew/frost formation at the surface. It also impacts clouds with low ice crystal number concentration, which is noticed by the aircraft observations of ice crystals in clear air. Braham and Spyers-Duran (1967) observed the ice crystals falling from cirrus trails and found that the cirrus crystals with length ~850 μm survived a fall of ~6 km in a dry environment. Such a long fall of kilometers is not explained well by the classic ice crystal sublimation rate with no REM (i.e., H_{ic} = 1). After introducing REM, the ice crystal sublimation rate is decreased by $(H_i - 1)/(H_i - H_{ic})$ times. For example, $(H_i - 1)/(H_i - H_{ic}) \approx 1.4$ when H_i = 0.3, η_z = 0.7 (over the lower-tropospheric clouds; Zeng 2018b), and H_{ic} = 0.8 (for HOICs in Fig. 1). Hence, REM can increase the computed fall distance significantly to match the observed one, supporting the mode.

- Mode II deals with the water transfer from small to large ice crystals; from vertically oriented (or spherical rosette) to horizontally oriented ice crystals, which resemble the Wegener–Bergeron–Findeisen process on the water transfer from supercooled drops to ice crystals (Zeng 2008, 2018a). The mode happens in an almost stationary air parcel, where H_i is modulated mainly by the sublimation/deposition of ice crystals, and consequently, large HOICs form at the expense of small (or vertically oriented) ice crystals. Figure 2 displays the formation of precipitating HOICs in a stationary air parcel with $\eta_z = 0.5$, temperature $T = -30$°C, and pressure $p = 680$ hPa, given the same initial spectra of vertically and horizontally oriented ice crystals.
- Mode III happens in an ascending air parcel near cloud top, where large HOICs grow fast while small ones need no sublimation to supply water vapor because additional water vapor for deposition is furnished via the adiabatic temperature decrease of ascending air (Zeng et al. 2021). The mode can be treated mathematically as a superimposition of modes I and II.

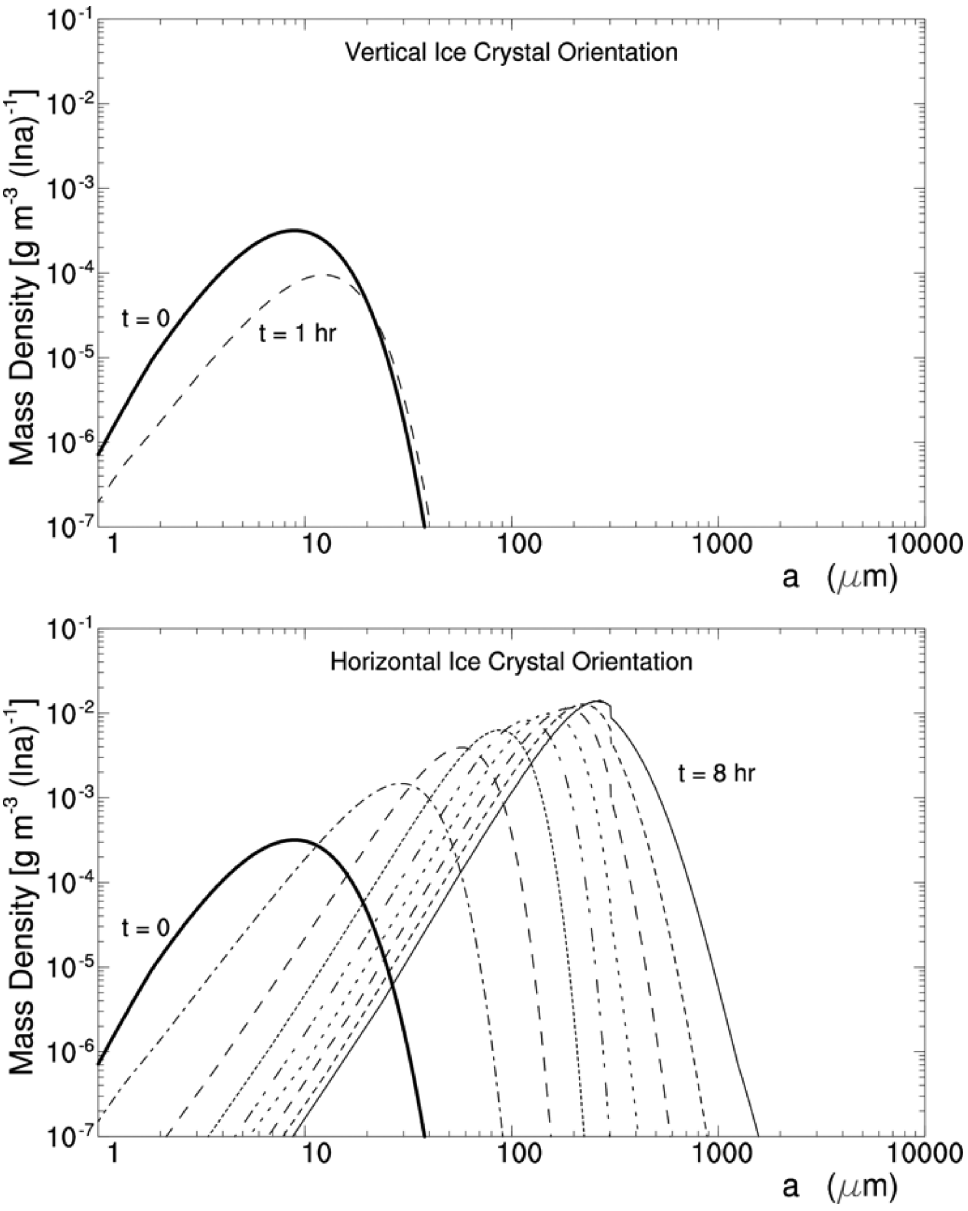

Fig. 2. REM-induced evolution of the spectrum $dM(\ln a)/d\ln a$ of (top) vertically and (bottom) horizontally oriented plate crystals, where $M(\ln a)$ denotes the mass of ice crystals with semi-major axis length shorter than a. Thick line denotes the initial spectrum; time interval between lines is 1 h. The simulation employs $\eta_z = 0.5$, $T = -30$°C, and $p = 680$ hPa (from Zeng 2018a).

REM with radiative warming. An air parcel with $\eta_z > 1$ is colloidally stable. When $\eta_z > 1$, $T_s > T$ and thus $H_{ic} > 1$ [see Eq. (7)]. Hence, radiative warming slows (or enhances) the deposition (or sublimation) of individual ice crystals. Consider multiple ice crystals in a stationary air parcel with $\eta_z > 1$. Their spectrum evolution relies on H_{ic}. Since $(H_{ic} - 1)/(\eta_z - 1)$ is a function of ice crystal size, shape, and orientation (Zeng 2008, 2018a), H_{ic} with $\eta_z > 1$ and < 1 is symmetric with respect to $H_{ic} = 1$ in Fig. 1. $H_{ic} - 1$ with $\eta_z = 1.5$, for example, is equal to $1 - (H_{ic} - 1)$ with $\eta_z = 0.5$. Hence, Fig. 1 (or Fig. 1 of Zeng 2018a) shows that H_{ic} with $\eta_z > 1$ increases with ice crystal size. The dependence of H_{ic} on crystal size at $\eta_z > 1$ explains the phenomenon in a stationary air parcel with $\eta_z > 1$: large ice crystals shrink via sublimation whereas small ones grow via deposition, narrowing the ice crystal spectrum (Wu et al. 2000; Zeng 2008).

Global distribution of radiative cooling/warming. Radiative cooling/warming plays a key role in REM and is measured by η_z. It has two contributors: clouds and their background. To distinguish the contributor of clouds from the other, η_z is decomposed into two parts:

$$\eta_z = \left(\eta_z\right)_{\text{background}} + \left(\eta_z\right)_{\text{cloud}}, \tag{8}$$

where $(\eta_z)_{\text{background}}$ represents η_z with no cloud and $(\eta_z)_{\text{cloud}}$ a perturbation of η_z imposed by clouds (Zeng et al. 2021).

The two parts in Eq. (8) are computed using Eq. (5), a two-stream radiation package for F^+ and F^-, and the observational data of the atmosphere, underlying surface, and clouds (Fu and Liou 1992; Chou et al. 1995; Zeng et al. 2021). The first part, $(\eta_z)_{\text{background}}$, is computed herein using the National Oceanic and Atmospheric Administration reanalysis data (see supplemental material for details). Its results are displayed in Fig. 3. Generally speaking, $\eta_z < 1$ in the lower and middle troposphere in the low and middle latitudes; $\eta_z < 1$ through the troposphere in the high latitudes, especially in Antarctica.

The other part, $(\eta_z)_{\text{cloud}}$, is determined by optically thick clouds, where thick and thin clouds are distinguished with a threshold of IR cloud optical depth of ~0.5 approximately. Figure 4, for example, displays η_z around a thick cloud, exhibiting a dipole structure of η_z: $\eta_z < 1$ near cloud top and $\eta_z > 1$ near bottom. The dipole structure is clear in physics. The ice crystals near cloud top and bottom receive almost the same upward and downward IR (or $\sim\sigma T^4$) from a thick cloud, respectively. However, the former receives little IR from the space and the air above, whereas the latter receives strong upwelling IR from the underlying surface, bringing about $\eta_z < 1$ near cloud top and $\eta_z > 1$ near bottom (Zeng 2008).

Although the accurate η_z of a specific cloud is obtained with in situ observational data (Zeng et al. 2021), Fig. 3 approximately represents the global distribution of η_z for thin clouds or clear sky and Fig. 4 for single-layer thick clouds when cloud bottom temperature is lower than the underlying surface temperature.

Global observations of REM

Since large and/or horizontally oriented ice crystals form at $\eta_z < 1$ via REM [see Eq. (7) for reason and Fig. 2 for crystal orientation selection], their observations are used to evaluate REM. The observations of polar clouds are discussed first, because $\eta_z < 1$ occurs frequently in the polar regions (Fig. 3).

Polar clouds. Diamond dust (or clear-sky precipitation) is common, especially in polar winter (Curry et al. 1996; Intrieri and Shupe 2004; Schlenczek et al. 2017). It consists of large ice crystals with diameters between 50 and 250 μm and occasionally near 1,000 μm (Shimizu 1963; Kikuchi and Hogan 1979; Walden et al. 2003; Lawson et al. 2006). In addition, its

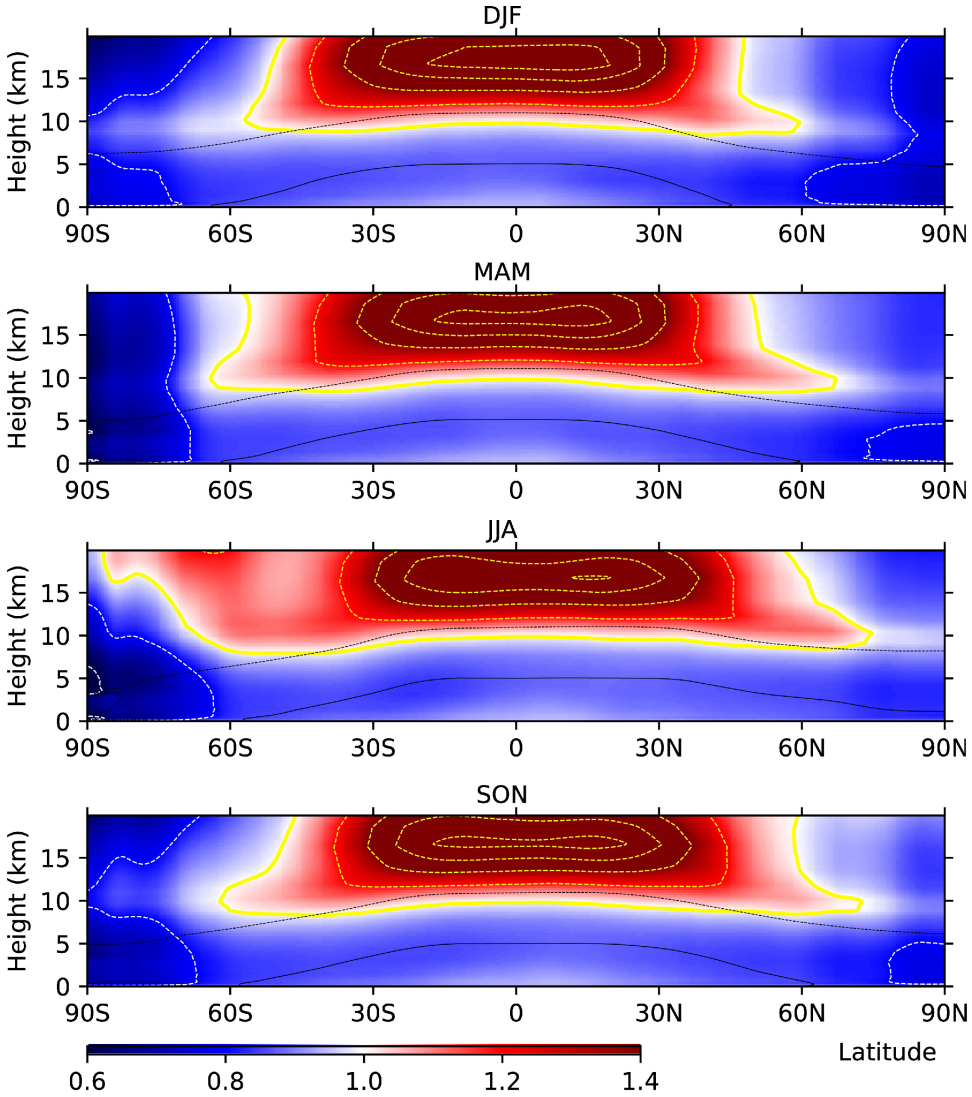

Fig. 3. Vertical cross section of the radiative ratio η_z with no clouds $(\eta_z)_{\text{background}}$ for the four seasons of 2019: (from top to bottom) December–February (DJF), March–May (MAM), June–August (JJA), and September–November (SON). Blue and red represent radiative cooling and warming, respectively; the yellow solid contour line denotes $\eta_z = 1$; the interval of η_z between the two contour lines is 0.2. Black solid and dashed lines denote the contour lines of air temperature $T = 0°$ and –40°C, respectively.

crystal number concentration and extinction are quite low. Thus, looking through diamond dust toward the Sun, an observer can see ice crystals falling just like diamonds—and away from the Sun, nothing except for blue sky. Hence, diamond dust differs from ice fog for its large crystal diameter and low crystal number concentration, because ice fog is "composed of suspended particles of ice, partly ice crystals 20–100 μm in diameter, but chiefly, especially when dense, droxtals 12–20 μm in diameter" (American Meteorological Society 2022).

Diamond dust and ice fog share two processes: REM and the overall cooling of air, where the latter process includes the heat flow from air to cooled crystals (Gotaas and Benson 1965). However, they are dominated by the two processes, respectively, because REM varies with crystal size (Fig. 1). In ice fog, all ice crystals have relatively weak REM because of their small size, and thus the overall cooling of air brings about $H_i > 1$ (or the air is supersaturated with respect to ice). In contrast, in diamond dust, ice crystals have strong REM for their large size, and larger crystals grow at the expense of water vapor so that $H_i < 1$, bringing about sublimation of smaller ice crystals (Zeng 2018a; see the modeled difference between ice fog and diamond dust in the supplemental material).

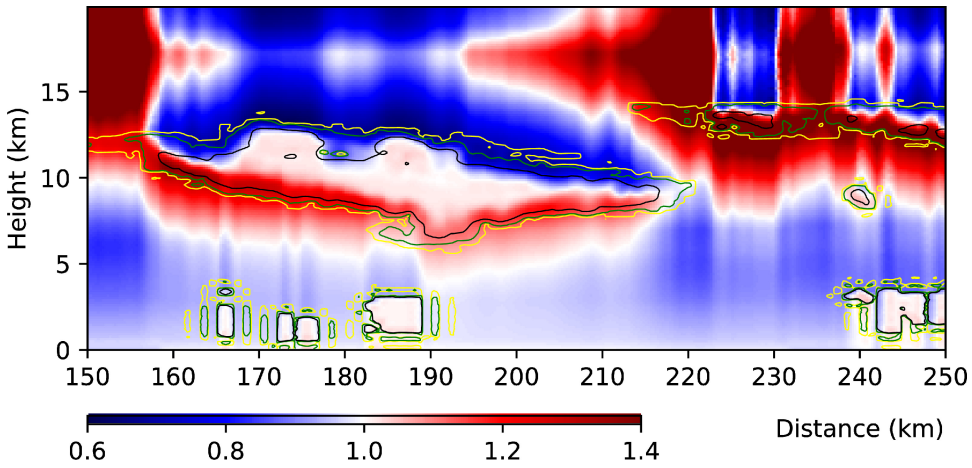

Fig. 4. Vertical cross sections of η_z in the cloudy atmosphere over the tropical Atlantic Ocean at 1506 UTC 11 Feb 2017. Blue and red represent radiative cooling and warming, respectively. Yellow, green, and black contour lines indicate the ice and liquid water content of 0.5 × 10⁻³, 5 × 10⁻³, and 50 × 10⁻³ g kg⁻¹, respectively. All data used come from the *CloudSat* and *CALIPSO* observations.

REM explains the thin column crystals of length ~1,000 μm (or the Shimizu crystals) observed in unsaturated environment. Consider an air parcel with relative humidity $H_i < 1$. Its ice crystals at equilibrium with half crystal size a^* satisfy $H_{ic} = H_i$. Figure 5 shows that a^* increases with decreasing H_i.

The magnitude of a^* is used to separate all ice crystals in the parcel into two subpopulations: small crystals with half crystal size $a < a^*$ that sublimate for their $H_{ic} > H_i$, and large ones with $a > a^*$ that grow for $H_{ic} < H_i$. Hence, in a special unsaturated environment with high H_i (or small a^*), an ice crystal grows and maintains $a > a^*$ during its descent. Once its size reaches ~100 μm, it grows rapidly to become a Shimizu crystal of length ~1,000 μm, because the H_{ic} of large ice crystals is far below 100% and decreases significantly with crystal size (Fig. 5).

REM also explains the vertical structure of diamond dust. Ice crystals of diamond dust usually originate in thin cirrus clouds above (Hogan 1975). After they fall into an unsaturated environment (or their mother cloud becomes dissipated), their spectrum is broadened and their number concentration is decreased by REM. This model of REM is consistent with the airborne observations of diamond

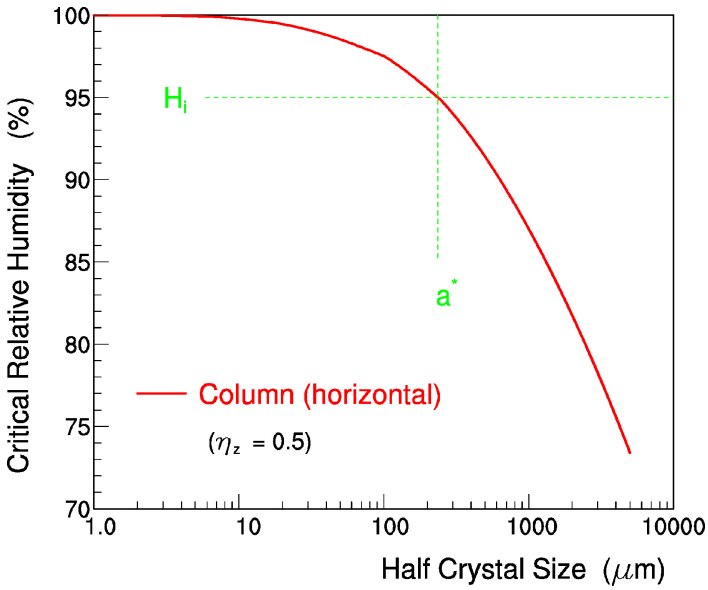

Fig. 5. Plot showing that an air parcel with η_z < 1 is colloidally unstable. Red line represents the critical relative humidity H_{ic} vs half crystal size (or semi-major axis length) a for horizontally oriented column-like crystals at η_z = 0.5, T = –30°C, and p = 680 hPa; it also represents the critical half crystal size a^* vs relative humidity H_i. Consider an air parcel with two ice crystals, H_i = 95%, and a^* = 235 μm (green lines). One crystal with a (e.g., 235.5 μm) > a^* grows via deposition and then maintains $H_{ic} < H_i$, becoming a precipitating particle eventually. In contrast, the other crystal with a (e.g., 234.5 μm) < a^* shrinks via sublimation and then maintains $H_{ic} > H_i$, vanishing eventually. As a result, the two crystals deviate from their initial size oppositely, showing the air parcel is colloidally unstable.

dust: the ice crystals at 900-m altitude above the ground were smaller and their number concentration was higher than toward lower altitudes (Ohtake et al. 1982).

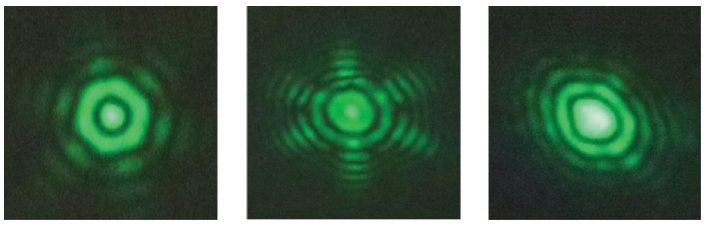

Fig. 6. Reflection images of three horizontally oriented ice crystals aloft on a grounded-based camera, which are (left) hexagonal plate with diameter 150 μm, (center) slightly rounded hexagonal plate with diameter 130 μm, and (right) strongly rounded hexagonal plate with diameter 120 μm. The images were photographed at the Summit Station in Greenland on 6 Dec 2016. Adapted from Goerke et al. (2017).

Two-dimensional reflections of a lidar beam were used to measure ice crystal properties, providing direct evidence to support REM (Goerke et al. 2017). When an ice crystal reflects a beam from a ground lidar onto the snow surface below, its specular reflection pattern is captured as an image by a camera. The image pattern, in turn, is used to retrieve its shape, size, orientation, roughness, and altitude, based on scattering theory (Ulanowski et al. 2012).

Figure 6, for example, displays three image patterns observed at the Summit Station in Greenland on 6 December 2016 (Goerke et al. 2017). The three patterns, as retrieved with the technique based on laser speckle (Ulanowski et al. 2012), are caused by three HOICs: a hexagonal plate with diameter 150 μm, a slightly rounded hexagonal plate with diameter 130 μm, and a strongly rounded hexagonal plate with diameter 120 μm, respectively. The retrieved shapes of the crystals reveal their histories: the hexagonal plate had undergone deposition; rounded crystals, sublimation (Nelson 1998).

Of all the ice crystals observed in Goerke et al. (2017), about half of the plates had evidence of rounding (implying sublimation). Other, larger ones, displayed pronounced optical speckle. The population was bimodal: small plates between 125 and 530 μm in size had undergone sublimation; large plates from 0.7 to 4.0 mm, deposition. Recent research has indicated that ice crystals producing significant speckle are characterized by the presence of geometric irregularities ("roughness") that are likely to be the result of fast and/or repeated (cyclic) growth (Voigtländer et al. 2018). Thus, the coexistence of two distinct subpopulations supports the separation of small and large crystals in Fig. 5 or mode II of REM.

The Cloud, Aerosol Polarization, and Backscatter Lidar (CAPABL) was developed to measure HOICs by implementing new polarization methods (Neely et al. 2013). CAPABL measures the particle backscatter ratio, the linear depolarization ratio, and a new data product called diattenuation through the combination of three polarization channels. The diattenuation, representing a polarization-dependent scattering efficiency, is contributed by HOICs instead of randomly oriented particles when viewed at oblique scattering angles (Hayman and Thayer 2012).

CAPABL was used to measure diattenuation with a beam zenith angle of 32° at Summit on 6 December 2016 (Neely et al. 2013, 2018; Goerke et al. 2017). Figure 7 displays its diattenuation, where strong diattenuation (red color) is contributed by HOICs. The figure also displays the corresponding radar reflectivity collected by the collocated Doppler, 35-GHz, millimeter cloud radar (MMCR) (Shupe et al. 2013). Although CAPABL rarely observed the cloud top (~5-km altitude) due to attenuation, its observed diattenuation still shows the existence of HOICs in the middle of the cloud (~2.5 km) that either form there or sediments from the upper portion of the cloud (or 3–5 km), supporting that REM is strong near the top or in the upper portion of thick clouds (or Fig. 4).

Optically thin ice clouds. Subvisual cirrus clouds are common in the tropical tropopause layer (TTL) (Heymsfield 1986). They consist of small ice crystals with low temperature

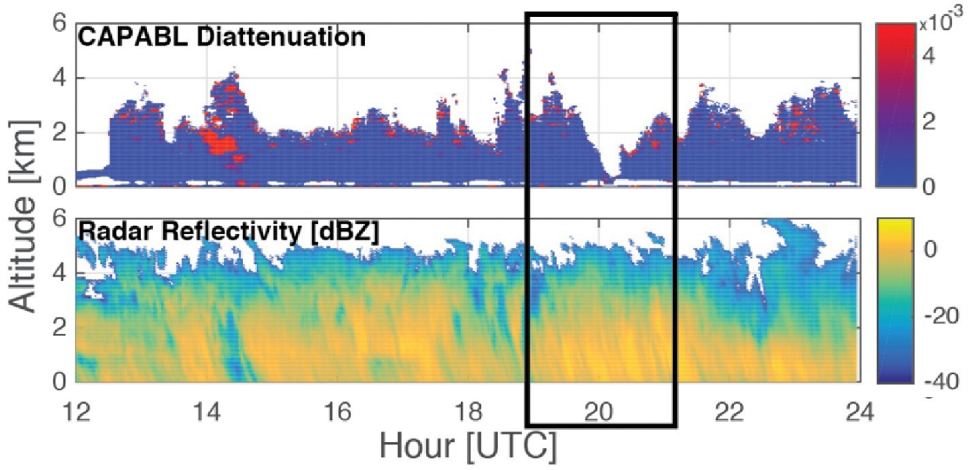

Fig. 7. (top) CAPABL diattenuation and (bottom) MMCR radar reflectivity at the Summit Station from 1200 to 2400 UTC 6 Dec 2016. Black box highlights the period of camera imaging in Fig. 6, and red denotes the contribution of HOICs. Adapted from Goerke et al. (2017).

(or ~−80°C) and low number concentration (McFarquhar et al. 2000). They are physically separated from cirrus below but tend to occur with cirrus below (Heymsfield 1986; Winker and Trepte 1998; Schwartz and Mace 2010). They can persist for weeks or months in clear skies in the equatorial regions (Lynch and Sassen 2002).

A challenging question is why the crystal number concentration in TTL is so low (Fig. 8; Heymsfield et al. 2013). Since ice nuclei (IN) become active with decreasing air temperature (Demott et al. 2010), it is expected that the number concentration of active IN at ~−80°C is very high. However, the observed crystal number concentration in TTL is quite low (Fig. 8). This significant discrepancy in number concentration between ice crystals and active IN suggests that most active IN do not grow up,[3] providing room for REM as an explanation.

REM with $\eta_z < 1$ can bring about the growth/shrinkage of relatively large/small crystals and subsequently a decrease in crystal number concentration, where active IN do not grow just like small ice crystals (Fig. 5; Zeng 2008). As a result, REM breaks the connection in number concentration between ice crystals and active IN, explaining why the number concentration of ice crystals is much lower than that of active IN in TTL.

On the other hand, $\eta_z < 1$ in TTL occurs only in company with thick clouds below because thick clouds block the strong upwelling IR from the surface (Fig. 9). The dependence of $\eta_z < 1$ in TTL on thick clouds below explains the correlation between subvisual cirrus clouds and thick clouds below.

Thin cirrus clouds are observed globally by a spaceborne lidar: the Cloud–Aerosol Lidar with Orthogonal Polarization (CALIOP) on the *Cloud–Aerosol Lidar and Infrared Pathfinder Satellite Observation* (*CALIPSO*) platform (Winker et al. 2010). Their HOICs are retrieved with CALIOP layer-integrated backscatter and depolarization ratio. Their CALIOP data reveal that HOICs are rare in optically thin ice clouds. Specifically, ~6% of optically thin ice cloud layers contain HOICs; within those layers, less than 5% of crystals are horizontally oriented (Noel and Chepfer 2010).

Furthermore, the percentage of clouds with HOICs increases with latitude (Noel and Chepfer 2010; Kikuchi et al. 2021). Most HOICs are found in thin cirrus clouds with temperatures warmer than −30°C (or altitude below 10 km); almost none with temperatures colder than −30°C (or altitude above 10 km) (Noel and Chepfer 2010; Zhou et al. 2012; Kikuchi et al. 2021). REM explains these phenomena with the spatial distribution of η_z. Since thin clouds below

[3] An active IN can initiate the ice phase at its active sites on a substrate surface. In spite of the capability for nucleation, it remains its original size if $H_i \le H_{ic}$. In an air parcel in TTL with $\eta_z < 1$, relatively large ice crystals grow at the expense of water vapor so that $H_i < H_{ic}$ for active IN, bringing about no growth of active IN. As a result, the active IN look like inactive ones.

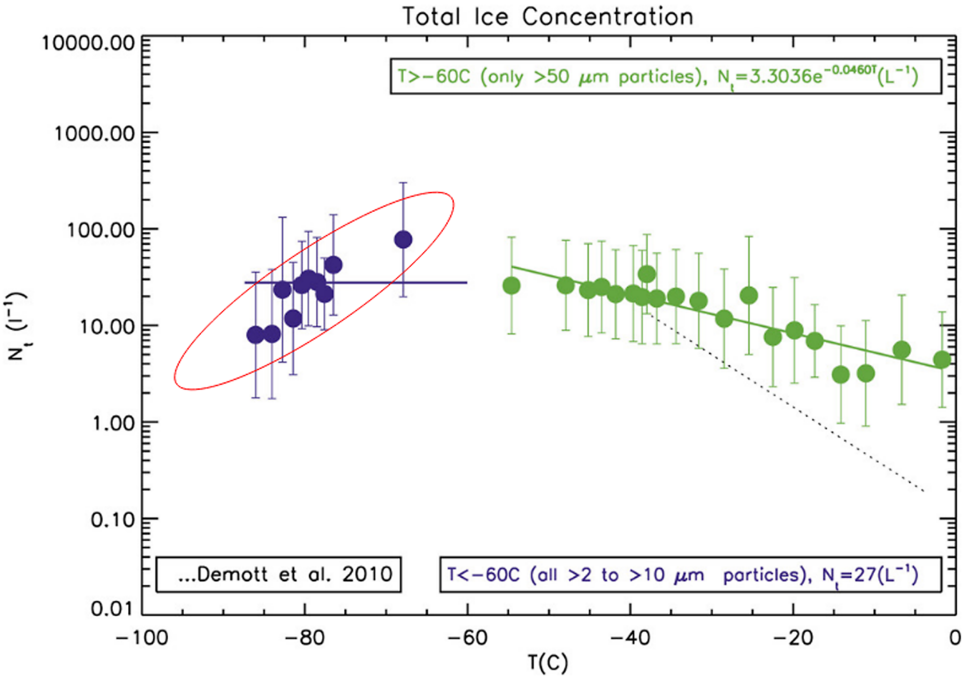

Fig. 8. Observed total ice crystal number concentrations N_t above 2–10 μm for T < –60°C (blue) and approximately 50 μm for T > –60°C (green) vs air temperature T, where solid lines represent data fitting, and the dotted line the average curve developed by Demott et al. (2010). Adapted from Heymsfield et al. (2013).

10 km usually undergo radiative cooling (or $\eta_z < 1$) (Fig. 3), HOICs form via REM; above 10 km, no HOICs form for radiative warming (or $\eta_z > 1$). In addition, the increase of HOICs with latitude is explained by the decrease of η_z with latitude (Fig. 3).

REM also explains why HOICs are rare in thin cirrus clouds but not in thick anvil clouds (Zeng et al. 2021). When $\eta_z < 1$, HOICs grow faster and faster because H_{ic} decreases with crystal size (Fig. 5). After becoming large, HOICs stay in their cloud if the cloud has a strong vertical velocity to support them; otherwise, they fall off their cloud. Since thin clouds usually possess small vertical velocity, they retain rare HOICs because most HOICs grow and then fall off, which explains the CALIOP observations of rare HOICs in thin cirrus clouds.

Optically thick ice clouds. HOICs in thick clouds are observed globally with a spaceborne microwave imager: the Global Precipitation Measurement (GPM) Microwave Imager (GMI) (Skofronick-Jackson et al. 2015). GMI uses 13 microwave channels to sense clouds, 10 of which take both horizontally (H) and vertically (V) polarized measurements at frequencies 10.65, 18.7, 36.5, 89, and 166 GHz. Its high-frequency channels of 166H and 166V are sensitive to ice crystal scattering, and its polarization difference at 166 GHz (or 166PD) is

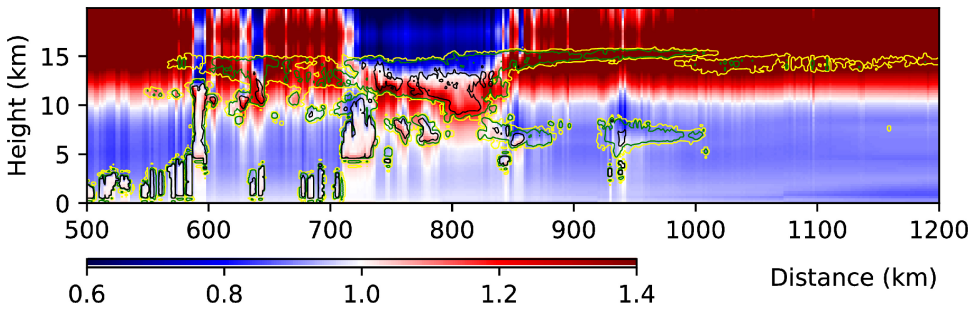

Fig. 9. As in Fig. 4, but for distance, where η_z < 1 (blue) near TTL occurs in company with the upper-tropospheric thick clouds below (enclosed by black lines).

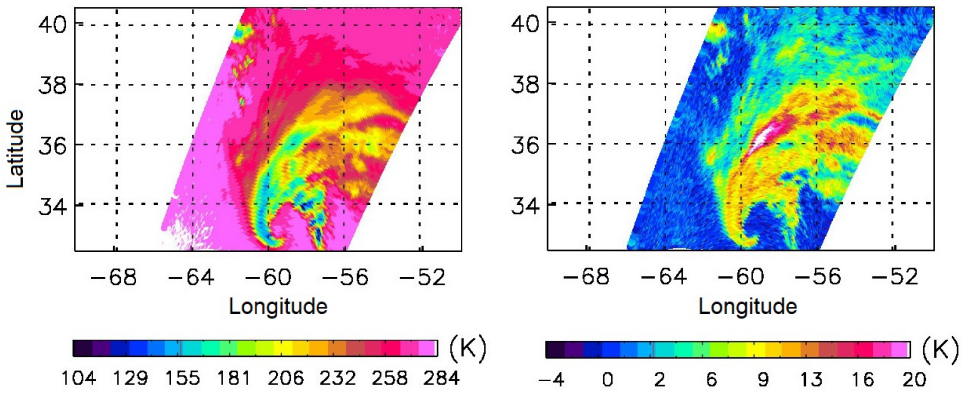

Fig. 10. Spatial distributions of (left) GMI TB and (right) PD at 166 GHz over a midlatitude winter frontal system at ~2000 UTC 25 Nov 2018, where TB represents average of the horizontally and vertically polarized measurements at 166 GHz. The inconsistency in spatial variation between TB and PD indicates that the percentage of HOICs varies spatially.

caused mainly by the ice crystal orientation near cloud top, where 166PD is defined as the difference in brightness temperature (TB) between vertically and horizontally polarized channel radiance measurements (Skofronick-Jackson et al. 2008; Roberti and Kummerow 1999; Adams et al. 2008; Defer et al. 2014). In other words, the magnitude of 166PD represents the contribution of HOICs near cloud top, given that other ice microphysical properties (e.g., size, habit) are statistically homogeneous on a pixel scale of 4.4×7.2 km^2 (Gong et al. 2018; Zeng et al. 2019). Figure 10, for example, displays GMI TB and PD at 166 GHz over a midlatitudinal winter frontal system, showing that HOICs are common. The inconsistency in spatial variation between TB and PD indicates that the percentage of HOICs varies highly in space.

Statistical analyses of GMI 166PD also show that HOICs in thick clouds are common from the low to high latitudes. Figure 11 displays the probability distribution functions (PDFs) of GMI 166PD over thick clouds and no clouds. Since the difference in PDF between thick clouds and no clouds is caused by thick clouds, the figure shows that thick clouds contribute ~3 K to 166PD from the low to high latitudes, indicating HOICs are common in thick clouds. This result is supported by the recent Polarimetric Radio Occultation observations

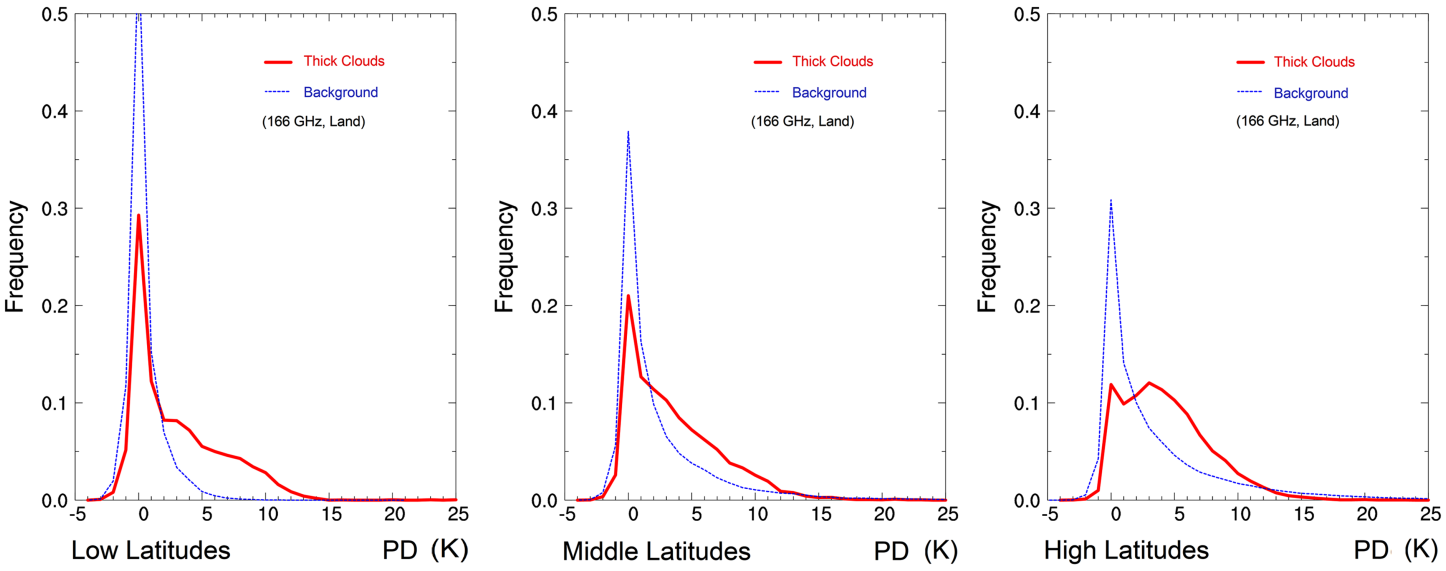

Fig. 11. PDF of the GMI 166PD (or polarization difference ΔT_b at 166 GHz) over land. Thick lines represent columns with the maximum radar reflectivity at 5–20 dB*Z* and thin ones with the maximum radar reflectivity below –20 dB*Z* (referred to as background) in the (left) low, (center) middle, and (right) high latitudes. Adapted from Zeng et al. (2019).

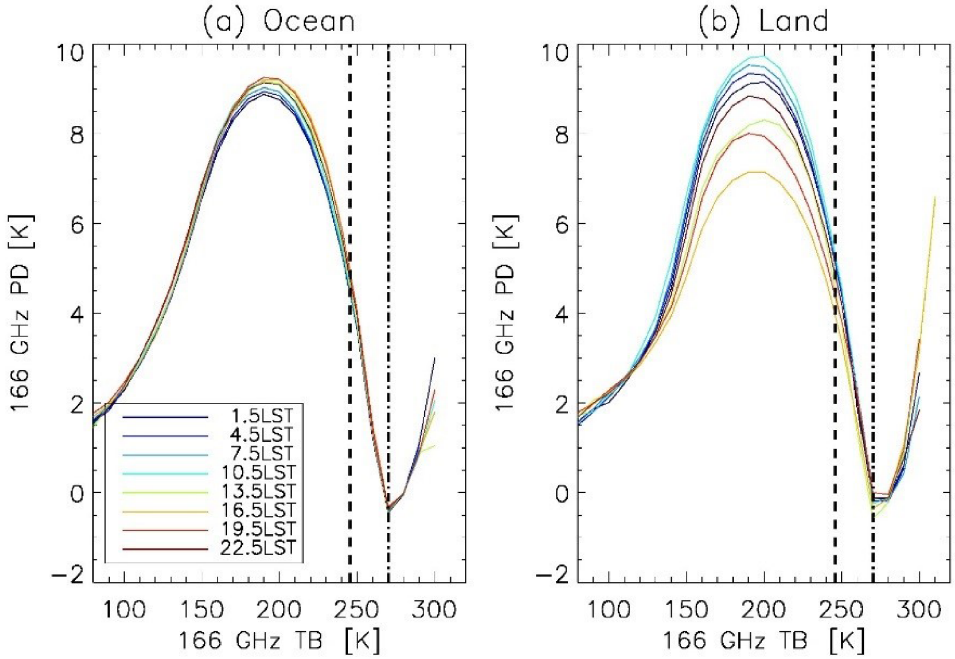

Fig. 12. Diurnal variation of GMI 166 PD over the (a) oceans and (b) land in the tropics (or between 30°S and 30°N), where the horizontal axis is TB from the vertically polarized channel radiance measurement at 166 GHz. A curve at a local solar time (LST), denoted by one color, connects the mean values of GMI 166PD in the TB bins at a given LST. The part to the left of the vertical dash–dotted line represents the contribution of the underlying surface; the part between the two vertical lines represents the contribution of the surface and thin clouds (from Gong et al. 2018).

(Padullés et al. 2021) and is consistent with the prediction of REM (or Fig. 4) concerning the latitude independence of HOICs in thick clouds.

In addition, GMI 166PD decreases with increasing cloud top height (or decreasing TB from 180 to 90 K in Fig. 12; Gong et al. 2018; Zeng et al. 2021). This phenomenon is explained by the sensitivity of REM to altitude in Fig. 13. GMI 166PD also exhibits a clear diurnal variation over tropical land (Fig. 12). It reaches the maximum at 0900 LST and minimum at 1500 LST, which is out of phase with cloud fraction (or the maximum at 1800 LST and minimum at 1100 LST). REM explains its diurnal variation with the diurnal variation of η_z. To be specific, the diurnal variation of η_z is caused by the diurnal variation of land surface temperature via F^+, reaching the lowest near dawn and highest after noon. After considering a delay of ~2 h for ice crystal growth, η_z coincides with GMI 166PD in phase. In contrast, GMI 166PD exhibits no obvious diurnal variation over the tropical oceans, because the sea surface temperature and thus η_z have weak diurnal variations. These coincidences in phase and magnitude between η_z and GMI 166PD suggest that REM brings about HOICs near cloud top.

Moreover, REM explains the strongest diurnal variation of GMI 166PD at TB ≈ 200 K over tropical land (Fig. 12). The coincident data of GMI and *CloudSat* reveal that the diurnal variation is contributed mainly by the clouds at ~7-km altitude (Gong et al. 2021); theoretical studies reveal the time scale of REM increases greatly with altitude and is about 24 h at ~7 km (Fig. 13). When the time scale of REM is close to the period of η_z, REM becomes strongest (Zeng 2008), which explains why the diurnal variation of GMI 166PD is strong at TB ≈ 200 K.

REM in warm clouds

Physics in warm clouds. REM is effective in warm fog/clouds just as in ice clouds because the atmosphere is quasi-transparent for IR with wavelengths of 8–12 μm (see Table 2; Roach 1976;

Barkstrom 1978). On the other hand, REM in warm clouds is weaker than in ice clouds, because ice crystals usually have aspect ratio away from one compared to liquid drops (see footnote 1 for the connection between size and aspect ratio of a nonspherical ice crystal; Zeng 2008).

REM in warm clouds, following Eq. (1), is measured by the critical relative humidity for a drop with radius r and salt mass m_s or

$$H_{wc} = E_{swn}\left(T_s, r, m_s\right) \Big/ E_{sw}\left(T\right), \tag{10}$$

where $E_{sw}(T)$ is the saturation vapor pressure over water at air temperature T and $E_{swn}(T_s, r, m_s)$ is the saturation vapor pressure around a drop at drop temperature T_s. Figure 14 displays H_{wc} against r and η_z, showing H_{wc} decreases with r when $\eta_z < 1$ and r is so large that the solute and surface effects are negligible.

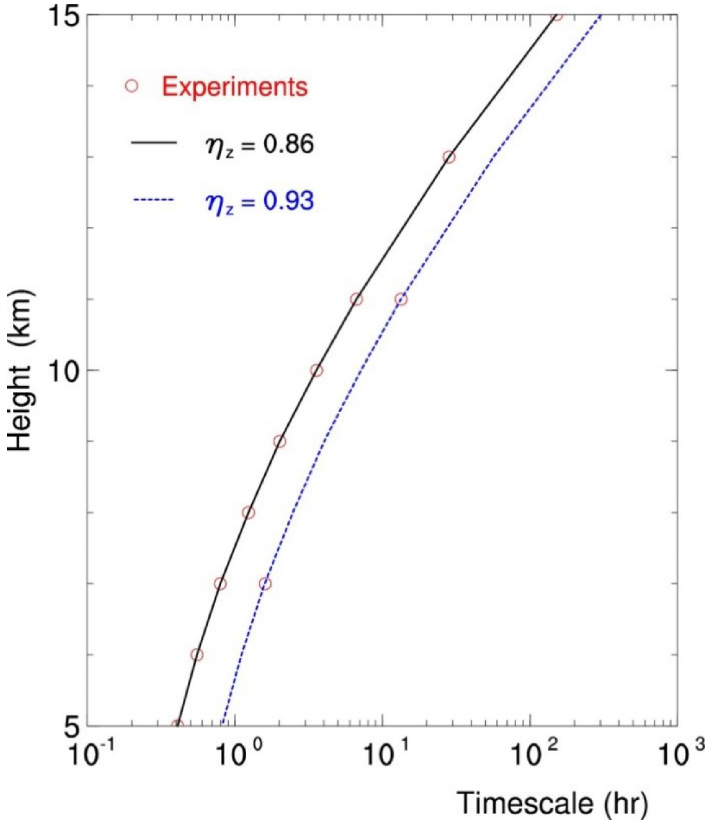

Fig. 13. Time scale of REM vs height at η_z = 0.86 (black) and 0.93 (blue) in the tropics. Red circles denote the results from the numerical experiments with explicit bin model simulation. The time scale represents a period for ice crystals to double their average size, and thus measures the REM-induced broadening of ice crystal spectrum (from Zeng et al. 2021).

Consider multiple drops in an air parcel with $\eta_z < 1$ and relative humidity with respect to water H_w. Suppose that one of the drops with radius r^* satisfies $H_{wc} = H_w$. Thus, all the drops are separated into two subpopulations: small drops with radius $r < r^*$ that evaporate for their $H_{wc} > H_w$, and large ones with $r > r^*$ that grow for $H_{wc} < H_w$. As a result, their spectrum is broadened by REM (Guzzi and Rizzi 1980), which is displayed in Fig. 15.

The broadening of the drop spectrum is replicated recently in an experimental apparatus, where droplet mist is accommodated in a vertically oriented tube that is cooled artificially (Brewster et al. 2020). The mist in the tube undergoes two processes: REM and the overall cooling of air, where the latter includes the radiative cooling of vapor constituents (e.g., water vapor) of air and the heat flow from air to cooled droplets. Since the former broadens the drop spectrum and the latter narrows the spectrum (see supplemental materials for their opposite effects on drop spectrum), the observed broad drop spectrum indicates that the former is important or REM is responsible for the observed broadening of the drop spectrum.

The broadening of the drop spectrum is also supported by the field observations of shallow cumulus. Small and Chuang (2008) used the phase Doppler interferometer to measure the drop spectrum at different levels of shallow cumulus and found that the drop spectrum near cloud top is quite broad. The observed broad drop spectrum at cloud top is consistent with the prediction of REM near cloud top, because $\eta_z < 1$ always occurs near cumulus cloud top (Fig. 4; Zeng 2018b).[4]

[4] The observations of Small and Chuang (2008) were also explained by the entrainment-mixing processes and stochastic condensation (e.g., Telford 1996; Liu et al. 2002; Desai et al. 2019, 2021; Luo et al. 2020).

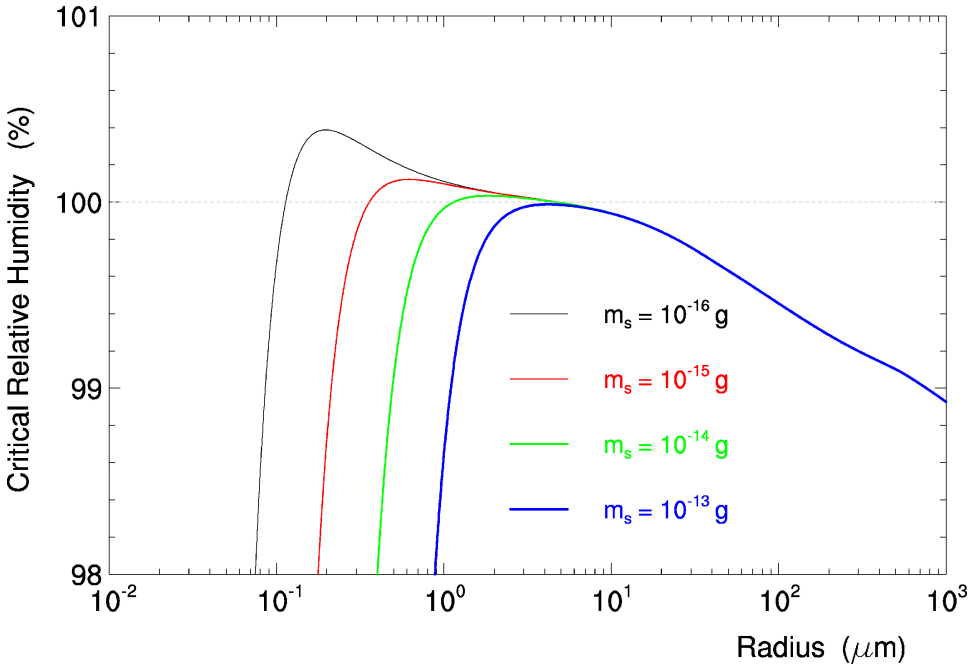

Fig. 14. Critical relative humidity H_{wc} of drops with different salt (NaCl) mass m_s vs radius at T = 15°C, p = 800 hPa, and η_z = 0.8.

In addition, solar radiation (SR) affects drop spectrum via REM and partially offsets the effect of IR (Hartman and Harrington 2005a,b; Marquis and Harrington 2005). To address its REM, SR can be introduced into Eq. (1) just as IR via η_z (Zeng 2018b). In warm clouds, SR heating dominates over IR cooling at larger drop radius (>200 μm), causing large drops to evaporate (Hartman and Harrington 2005a). Its REM decreases with solar zenith angle (Hartman and Harrington 2005b). In ice clouds, SR heating can cause large HOICs to sublimate and thus decrease the percentage of large HOICs, bringing about a diurnal variation of GMI 166PD with a minimum after noon, especially in the tropics. Figure 12 displays

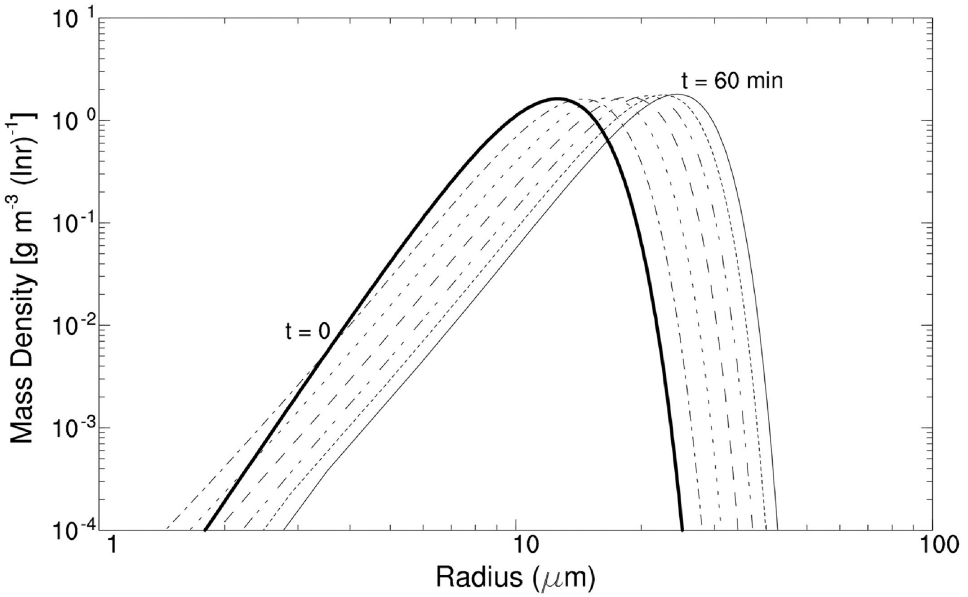

Fig. 15. REM-induced broadening of drop spectrum in an air parcel with η_z = 0.8, T = 15°C, and p = 800 hPa. The vertical axis is the mass density $dM(\ln r)/d\ln r$, where $M(\ln r)$ is the mass of drops with radius shorter than r. Thick line denotes the initial drop spectrum, and the time interval between lines is 10 min. The continuous spectrum shifting to larger sizes generates numerous large droplets (or drops with radius larger than 28 μm) eventually (from Zeng 2018b).

the diurnal variations of GMI 166PD over the tropical oceans and land, showing that the two diurnal variations are almost out of phase. Suppose that the diurnal variation over the tropical oceans is caused mainly by SR and the diurnal variation over tropical land by both IR and SR. The figure thus suggests that the SR-induced REM is about 1/6 (or less) of the IR-induced REM in magnitude.

Interaction between REM and other cloud processes. Clouds change η_z that in turn changes themselves and other clouds, which exhibits as an interaction between REM and other cloud processes. The interaction can be simulated using multiple-dimensional cloud models with bin microphysics, which is exampled below for fog and clouds, respectively.

The interaction between REM and gravitational drop settling impacts the life cycle of fog, which is replicated in the one-dimensional fog model of Bott et al. (1990). REM induces large droplets near fog top that in turn fall to the ground quickly, bringing about a strong reduction of liquid water content and therefore a change of radiative cooling rate. The phase shift between large droplet growth and radiative cooling rate then brings about an oscillation in liquid water content and radiative fluxes, which resembles an oscillation observed in fog with a period of 10–30 min (Bott et al. 1990).

REM near cloud top cooperates with drop collection, accelerating the rain initiation in warm clouds (Austin et al. 1995). Nevertheless, the effect of REM on rain initiation in an air parcel depends on the residence time of the parcel near cloud top or edge (Harrington et al. 2000; Klinger et al. 2019), which becomes complicated by involving condensation nuclei and turbulent mixing (Ackerman et al. 1995).

Outlook

REM predicts that large and/or horizontally oriented ice crystals form at $\eta_z < 1$.[5] Since its prediction is consistent with the plentiful observations of HOICs and other particle characteristics from different platforms (e.g., aircrafts, field campaigns, and satellites), it is inferred that REM exists from the Arctic to the tropics.

The current operational weather and climate models overlook REM, although they have represented the overall cooling of air, including the heat flow from air to cooled cloud particles (that is equal to the radiative cooling of cloud particles). If they incorporate REM in terms of η_z, their water cycle will be improved with the following scenarios:

- Excessive water vapor is mitigated by the REM-induced formation of precipitating ice crystals (e.g., diamond dust). The process is important in the polar regions, especially in Antarctica during wintertime.
- Excessive water vapor is mitigated by the REM-inhibited sublimation and enhanced sedimentation of precipitating ice crystals in subsaturated air. One example is the long survival of precipitating ice crystals in a dry environment observed by Braham and Spyers-Duran (1967).
- Variations of subvisual cirrus clouds in TTL are associated with cirrus clouds below via REM. As a result, REM can reduce the amount of water vapor that ascends from the troposphere to the stratosphere.
- Optically thick clouds are converted to thin ones via REM. Since $\eta_z < 1$ near thick cloud top, precipitating ice crystals

[5] Since REM favors the growth of HOICs and therefore increases the percentage of HOICs, it changes the percentage of HOICs independently of turbulence (Klett 1995), crystal shape (Stoelinga et al. 2007), and the process of Jayaweera and Mason (1965; hereafter JM), which is illustrated as follows. JM released cylinders into a liquid tank with random perturbation and then found the dominance of horizontally oriented cylinders. Suppose that JM knew the details of initial cylinder releasing and grouped the initial releasing into two kinds: one for horizontally oriented cylinders and the other for vertically oriented cylinders (even though the first kind has much more cylinders than the second kind). If JM redid two experiments with the two kinds of cylinder releasing, respectively, then they would see different cylinder orientations in the two experiments: all cylinders with the first kind of releasing are horizontally oriented and all cylinders with the second kind of releasing are vertically oriented. The difference in cylinder orientation between the two ideal experiments suggests that initial cylinder releasing can change the percentage of horizontally oriented cylinders. In clouds, REM functions similarly as the initial cylinder releasing while it does not affect the process of JM.

form there and then fall off until thick clouds become thin ones (or their dipole structure of η_z is gone). This interaction between REM and clouds is similar to that described in Bott et al. (1990).
- REM broadens the drop spectrum near the top of small cumulus that in turn helps the rain initiation of small cumulus (Austin et al. 1995; Harrington et al. 2000; Small and Chuang 2008; Zeng 2018b; Klinger et al. 2019).

In addition, HOICs have a smaller fall speed than other crystals (Heymsfield and Iaquinta 2000) and increase cloud albedo (Takano and Liou 1989).

In bulk, REM removes water vapor, liquid water, and ice from the atmosphere, working as a sink of water. It thus can impact climate change just as the release of carbon dioxide (CO_2) via greenhouse gas accumulation. Consider, for example, an ideal climate model that represents all processes accurately. If it excluded REM, its water content would become too high via accumulation and thus its predicted global warming too strong, which is estimated in comparison to CO_2. CO_2 increases its concentration from 360 ppm in 1995 to 410 ppm in 2019 (IPCC 2021), corresponding to a relative increase of 5.7×10^{-7}% day^{-1}. Thus, an equivalent change of water vapor in a vertical column is 2.9×10^{-4} g m^{-2} day^{-1} (if the precipitable water is represented with a tropical value of ~50 kg m^{-2}). Since dew/frost can remove water vapor from the atmosphere on the order of 2.9×10^{-4} g m^{-2} day^{-1} (or higher), REM is as important as the release of CO_2 in climate modeling.

To remove the excessive water and spurious warming, the current models usually introduce artificial sinks of water (e.g., the artificial adjustment of water vapor to observed relative humidity, the autoconversion of cloud ice to precipitating water), causing distortion of the water cycle. Specifically, the models maintain a quasi-balance between water sources and sinks by tuning the parameterization of clouds (or water sources), and consequently pass the errors of the sink representation into the parameterization of clouds. As a result, they generate water biases in one form or another, such as the low bias in supercooled liquid water in mixed-phase clouds (Klein et al. 2009; Komurcu et al. 2014) that may also be caused by lacking the subgrid parameterization of the Wegener–Bergeron–Findeisen process (Tan and Storelvmo 2016). If the models represented the water sink properly via REM, their parameterization of clouds could be improved or constrained "easily" by observations, because one side of the water balance was anchored. Hence, introducing REM will greatly improve the accuracy of the water and energy cycles of the atmosphere in the models.

Acknowledgments. The authors thank Dr. Manfred Wendisch (editor), Dr. Xianglei Huang, and three anonymous reviewers for their kind and constructive comments. They also thank Eric Mark and Jessica Schultheis for reading the manuscript.

References

Ackerman, A. S., P. V. Hobbs, and O. B. Toon, 1995: A model for particle microphysics, turbulent mixing, and radiative transfer in the stratocumulus-topped marine boundary layer and comparisons with measurements. *J. Atmos. Sci.*, **52**, 1204–1236, https://doi.org/10.1175/1520-0469(1995)052<1204:AMFPMT>2.0.CO;2.

Adams, I. S., P. Gaiser, and W. L. Jones, 2008: Simulation of the Stokes vector in inhomogeneous precipitation. *Radio Sci.*, **43**, RS5006, https://doi.org/10.1029/2007RS003744.

American Meteorological Society, 2022: Ice fog. Glossary of Meteorology, https://glossary.ametsoc.org/wiki/Ice_fog.

Auer, A. H., and D. L. Veal, 1970: The dimension of ice crystals in natural clouds. *J. Atmos. Sci.*, **27**, 919–926, https://doi.org/10.1175/1520-0469(1970)027<0919:TDOICI>2.0.CO;2.

Austin, P. H., S. Siems, and Y. Wang, 1995: Constraints on droplet growth in radiatively cooled stratocumulus clouds. *J. Geophys. Res.*, **100**, 14 231–14 242, https://doi.org/10.1029/95JD01268.

Barkstrom, B. R., 1978: Some effects of 8–12 μm radiant energy transfer on the mass and heat budgets of cloud droplets. *J. Atmos. Sci.*, **35**, 665–673, https://doi.org/10.1175/1520-0469(1978)035<0665:SEORET>2.0.CO;2.

Bott, A., U. Sievers, and W. Zdunkowski, 1990: A radiation fog model with a detailed treatment of the interaction between radiative transfer and fog microphysics. *J. Atmos. Sci.*, **47**, 2153–2166, https://doi.org/10.1175/1520-0469(1990)047<2153:ARFMWA>2.0.CO;2.

Braham, R. R., Jr., and P. Spyers-Duran, 1967: Survival of cirrus crystals in clear air. *J. Appl. Meteor.*, **6**, 1053–1061, https://doi.org/10.1175/1520-0450(1967)006<1053:SOCCIC>2.0.CO;2.

Brewster, M. Q., X. Li, K. K. Roman, E. O. McNichols, and M. J. Rood, 2020: Radiation-induced condensational growth and cooling of cloud-sized mist droplets. *J. Atmos. Sci.*, **77**, 3585–3600, https://doi.org/10.1175/JAS-D-19-0288.1.

Chou, M.-D., W. Ridgway, and M.-H. Yan, 1995: Parameterizations for water vapor IR radiative transfer in both the middle and lower atmosphere. *J. Atmos. Sci.*, **52**, 1159–1167, https://doi.org/10.1175/1520-0469(1995)052<1159:PFWVIR>2.0.CO;2.

Curry, J. A., J. L. Schramm, W. B. Rossow, and D. Randall, 1996: Overview of Arctic cloud and radiation characteristics. *J. Climate*, **9**, 1731–1764, https://doi.org/10.1175/1520-0442(1996)009<1731:OOACAR>2.0.CO;2.

Defer, E., V. S. Galligani, C. Prigent, and C. Jimenez, 2014: First observations of polarized scattering over ice clouds at close-to-millimeter wavelengths (157 GHz) with MADRAS on board the Megha-Tropiques mission. *J. Geophys. Res. Atmos.*, **119**, 12 301–12 316, https://doi.org/10.1002/2014JD022353.

Demott, P. J., and Coauthors, 2010: Predicting global atmospheric ice nuclei distributions and their impacts on climate. *Proc. Natl. Acad. Sci. USA*, **107**, 11 217–11 222, https://doi.org/10.1073/pnas.0910818107.

Desai, N., S. Glienke, J. Fugal, and R. A. Shaw, 2019: Search for microphysical signatures of stochastic condensation in marine boundary layer clouds using airborne digital holography. *J. Geophys. Res. Atmos.*, **124**, 2739–2752, https://doi.org/10.1029/2018JD029033.

——, Y. Liu, S. Glienke, R. A. Shaw, C. Lu, J. Wang, and S. Gao, 2021: Vertical variation of turbulent entrainment mixing processes in marine stratocumulus clouds using high resolution digital holography. *J. Geophys. Res. Atmos.*, **126**, e2020JD033527, https://doi.org/10.1029/2020JD033527.

Franklin, C. N., A. Protat, D. Leroy, and E. Fontaine, 2016: Controls on phase composition and ice water content in a convection-permitting model simulation of a tropical mesoscale convective system. *Atmos. Chem. Phys.*, **16**, 8767–8789, https://doi.org/10.5194/acp-16-8767-2016.

Fu, Q., and K.-N. Liou, 1992: On the correlated k-distribution method for radiative transfer in nonhomogeneous atmospheres. *J. Atmos. Sci.*, **49**, 2153–2170, https://doi.org/10.1175/1520-0469(1992)049<2139:OTCDMF>2.0.CO;2.

Fuchs, N. A., 1959: *Evaporation and Droplet Growth in Gaseous Media.* Pergamon Press, 72 pp.

Goerke, M., and Coauthors, 2017: Characterizing ice particles using two-dimensional reflections of a lidar beam. *Appl. Opt.*, **56**, G188–G196, https://doi.org/10.1364/AO.56.00G188.

Gong, J., X. Zeng, D. L. Wu, and X. Li, 2018: Diurnal variation of tropical ice cloud microphysics: Evidence from Global Precipitation Measurement Microwave Imager (GPM-GMI) polar metric measurements. *Geophys. Res. Lett.*, **45**, 1185–1193, https://doi.org/10.1002/2017GL075519.

——, and Coauthors, 2021: Linkage among ice crystal microphysics, mesoscale dynamics and cloud and precipitation structures revealed by collocated microwave radiometer and multi-frequency radar observations. *Atmos. Chem. Phys.*, **20**, 12 633–12 653, https://doi.org/10.5194/acp-20-12633-2020.

Gotaas, Y., and C. S. Benson, 1965: The effect of suspended ice crystals on radiative cooling. *J. Appl. Meteor.*, **4**, 446–453, https://doi.org/10.1175/1520-0450(1965)004<0446:TEOSIC>2.0.CO;2.

Guzzi, R., and R. Rizzi, 1980: The effect of radiative exchange on the growth of a population of droplets. *Contrib. Atmos. Phys.*, **53**, 351–365.

Hall, W. D., and H. R. Pruppacher, 1976: The survival of ice particles falling from cirrus clouds in subsaturated air. *J. Atmos. Sci.*, **33**, 1995–2006, https://doi.org/10.1175/1520-0469(1976)033<1995:TSOIPF>2.0.CO;2.

Harrington, J. Y., G. Feingold, and W. R. Cotton, 2000: Radiative impacts on the growth of a population of drops within simulated summertime Arctic stratus. *J. Atmos. Sci.*, **57**, 766–785, https://doi.org/10.1175/1520-0469(2000)057<0766:RIOTGO>2.0.CO;2.

Hartman, C. M., and J. Y. Harrington, 2005a: Radiative impacts on the growth of drops within simulated marine stratocumulus. Part I: Maximum solar heating. *J. Atmos. Sci.*, **62**, 2323–2338, https://doi.org/10.1175/JAS3477.1.

——, and ——, 2005b: Radiative impacts on the growth of drops within simulated marine stratocumulus. Part II: Solar zenith angle variations. *J. Atmos. Sci.*, **62**, 2339–2351, https://doi.org/10.1175/JAS3478.1.

Hayman, M., and J. P. Thayer, 2012: General description of polarization in lidar using Stokes vectors and polar decomposition of Mueller matrices. *J. Opt. Soc. Amer.*, **29A**, 400–409, https://doi.org/10.1364/JOSAA.29.000400.

Heymsfield, A., 1972: Ice crystal terminal velocities. *J. Atmos. Sci.*, **29**, 1348–1357, https://doi.org/10.1175/1520-0469(1972)029<1348:ICTV>2.0.CO;2.

——, 1973: Cirrus uncinus generating cells and the evolution of cirriform clouds. Ph.D. thesis, University of Chicago, 273 pp.

——, 1986: Ice particles observed in a cirriform cloud at –83°C and implications for polar stratospheric clouds. *J. Atmos. Sci.*, **43**, 851–855, https://doi.org/10.1175/1520-0469(1986)043<0851:IPOIAC>2.0.CO;2.

——, and J. Iaquinta, 2000: Cirrus crystal terminal velocities. *J. Atmos. Sci.*, **57**, 916–938, https://doi.org/10.1175/1520-0469(2000)057<0916:CCTV>2.0.CO;2.

——, C. Schmitt, and A. Bansemer, 2013: Ice cloud particle size distributions and pressure-dependent terminal velocities from in situ observations at temperatures from 0° to –86°C. *J. Atmos. Sci.*, **70**, 4123–4154, https://doi.org/10.1175/JAS-D-12-0124.1.

——, and Coauthors, 2017: Cirrus clouds. *Ice Formation and Evolution in Clouds and Precipitation: Measurement and Modeling Challenges*, *Meteor. Monogr.*, No. 58, Amer. Meteor. Soc., https://doi.org/10.1175/AMSMONOGRAPHS-D-16-0010.1.

Hogan, A. W., 1975: Summer ice crystal precipitation at the South Pole. *J. Appl. Meteor.*, **14**, 246–249, https://doi.org/10.1175/1520-0450(1975)014<0246:SICPAT>2.0.CO;2.

Intrieri, J. M., and M. D. Shupe, 2004: Characteristics and radiative effects of diamond dust over the western Arctic Ocean region. *J. Climate*, **17**, 2953–2960, https://doi.org/10.1175/1520-0442(2004)017<2953:CAREOD>2.0.CO;2.

IPCC, 2021: *Climate Change 2021: The Physical Science Basis.* V. Masson-Delmotte et al., Eds., Cambridge University Press, 2391 pp., https://www.ipcc.ch/report/ar6/wg1/downloads/report/IPCC_AR6_WGI_FullReport.pdf.

Jayaweera, K. O. L. F., and B. J. Mason, 1965: The behavior of freely falling cylinders and cones in a viscous fluid. *J. Fluid Mech.*, **22**, 709–720, https://doi.org/10.1017/S002211206500109X.

Jiang, J. H., and Coauthors, 2012: Evaluation of cloud and water vapor simulations in CMIP5 climate models using NASA "A-Train" satellite observations. *J. Geophys. Res.*, **117**, D14105, https://doi.org/10.1029/2011JD017237.

——, H. Su, C. Zhai, L. Wu, K. Minschwaner, A. M. Molod, and A. M. Tompkins, 2015: An assessment of upper troposphere and lower stratosphere water vapor in MERRA, MERRA2, and ECMWF re-analyses using Aura MLS observations. *J. Geophys. Res. Atmos.*, **120**, 11 468–11 485, https://doi.org/10.1002/2015JD023752.

Kikuchi, K., and A. W. Hogan, 1979: Properties of diamond dust type ice crystals observed in summer season at Amundsen-Scott South Pole Station, Antarctica. *J. Meteor. Soc. Japan*, **57**, 180–190, https://doi.org/10.2151/jmsj1965.57.2_180.

Kikuchi, M., H. Okamoto, and K. Sato, 2021: A climatological view of horizontal ice plates in clouds: Findings from nadir and off-nadir CALIPSO observations. *J. Geophys. Res. Atmos.*, **126**, e2020JD033562, https://doi.org/10.1029/2020JD033562.

Klein, S. A., and Coauthors, 2009: Intercomparison of model simulations of mixed-phase clouds observed during the ARM Mixed-Phase Arctic Cloud Experiment. I: Single-layer cloud. *Quart. J. Roy. Meteor. Soc.*, **135**, 979–1002, https://doi.org/10.1002/qj.416.

Klett, J. D., 1995: Orientation model for particles in turbulence. *J. Atmos. Sci.*, **52**, 2276–2285, https://doi.org/10.1175/1520-0469(1995)052<2276:OMFPIT>2.0.CO;2.

Klinger, C., G. Feingold, and T. Yamaguchi, 2019: Cloud droplet growth in shallow cumulus clouds considering 1D and 3D thermal radiative effects. *Atmos. Chem. Phys.*, **19**, 6295–6313, https://doi.org/10.5194/acp-2018-1204..

Komurcu, M., and Coauthors, 2014: Intercomparison of the cloud water phase among global climate models. *J. Geophys. Res. Atmos.*, **119**, 3372–3400, https://doi.org/10.1002/2013JD021119.

Lawson, R. P., B. A. Baker, P. Zmarzly, D. O'Connor, Q. Mo, J.-F. Gayet, and V. Shcherbakov, 2006: Microphysical and optical properties of atmospheric ice crystals at South Pole Station. *J. Appl. Meteor. Climatol.*, **45**, 1505–1524, https://doi.org/10.1175/JAM2421.1.

Lebo, Z., N. Johnson, and J. Harrington, 2008: Radiative influences on ice crystal and droplet growth within mixed-phase stratus clouds. *J. Geophys. Res.*, **113**, D09203, https://doi.org/10.1029/2007JD009262.

Liou, K. N., 1986: Influence of cirrus clouds on weather and climate processes: A global perspective. *Mon. Wea. Rev.*, **114**, 1167–1199, https://doi.org/10.1175/1520-0493(1986)114<1167:IOCCOW>2.0.CO;2.

Liu, Y., P. H. Daum, and J. Hallett, 2002: A generalized systems theory for the effect of varying fluctuation in cloud droplet size distributions. *J. Atmos. Sci.*, **59**, 2279–2289, https://doi.org/10.1175/1520-0469(2002)059<2279:AGSTFT>2.0.CO;2.

Luo, S., and Coauthors, 2020: Parameterizations of entrainment-mixing mechanisms and their effects on cloud droplet spectral width based on numerical simulations. *J. Geophys. Res. Atmos.*, **125**, e2020JD032972, https://doi.org/10.1029/2020JD032972.

Lynch, D. K., and K. Sassen, 2002: Subvisual cirrus. *Cirrus*, D. K. Lynch et al., eds., Oxford University Press, 256–264.

Marquis, J., and J. Y. Harrington, 2005: Radiative influences on drop and cloud condensation nuclei equilibrium in stratocumulus. *J. Geophys. Res.*, **110**, D10205, https://doi.org/10.1029/2004JD005401.

Mason, B. J., 1971: *The Physics of Clouds.* Clarendon Press, 671 pp.

McFarquhar, G. M., A. J. Heymsfield, J. Spinhirne, and B. Hart, 2000: Thin and subvisual tropopause tropical cirrus: Observations and radiative impacts. *J. Atmos. Sci.*, **57**, 1841–1853, https://doi.org/10.1175/1520-0469(2000)057<1841:TASTTC>2.0.CO;2.

Morrison, H., and Coauthors, 2011: Intercomparison of cloud model simulations of Arctic mixed-phase boundary layer clouds observed during SHEBA/FIRE-ACE. *J. Adv. Model. Earth Syst.*, **3**, M06003, https://doi.org/10.1029/2011MS000066.

Nam, C., S. Bony, J.-L. Dufresne, and H. Chepfer, 2012: The 'too few, too bright' tropical low-cloud problem in CMIP5 models. *Geophys. Res. Lett.*, **39**, L21801, https://doi.org/10.1029/2012GL053421.

Neely, R., M. Hayman, R. Stillwell, J. Thayer, R. Hardesty, M. O'Neill, M. Shupe, and C. Alvarez, 2013: Polarization lidar at Summit, Greenland, for the detection of cloud phase and particle orientation. *J. Atmos. Oceanic Technol.*, **30**, 1635–1655, https://doi.org/10.1175/JTECH-D-12-00101.1.

——, R. Stillwell, S. Cole, ——, M. Shupe, M. Goerke, S. Dorsi, and J. Ulanowski, 2018: Profiles of horizontally oriented ice crystals observed by polarization lidar over Summit, Greenland. *EPJ Web Conf.*, **176**, 05007, https://doi.org/10.1051/epjconf/201817605007.

Nelson, J., 1998: Sublimation of ice crystals. *J. Atmos. Sci.*, **55**, 910–919, https://doi.org/10.1175/1520-0469(1998)055<0910:SOIC>2.0.CO;2.

Noel, V., and H. Chepfer, 2010: A global view of horizontally oriented crystals in ice clouds from Cloud-Aerosol Lidar and Infrared Pathfinder Satellite Observation (CALIPSO). *J. Geophys. Res.*, **115**, D00H23, https://doi.org/10.1029/2009JD012365.

Ohtake, T., K. Jayaweera, and K.-I. Sakurai, 1982: Observation of ice crystal formation in lower Arctic atmosphere. *J. Atmos. Sci.*, **39**, 2898–2904, https://doi.org/10.1175/1520-0469(1982)039<2898:OOICFI>2.0.CO;2.

Padullés, R., E. Cardellach, F. J. Turk, C. O. Ao, M. de la Torre Juárez, J. Gong, and D. L. Wu, 2021: Sensing horizontally oriented frozen particles with polar metric radio occultation's aboard PAZ: Validation using GMI coincident observations and Cloudsat a-priori information. *IEEE Trans. Geosci. Remote Sens.*, **60**, 4101513, https://doi.org/10.1109/TGRS.2021.3065119.

Powell, S. W., R. A. Houze Jr., A. Kumar, and S. A. McFarlane, 2012: Comparison of simulated and observed continental tropical anvil clouds and their radiative heating profiles. *J. Atmos. Sci.*, **69**, 2662–2681, https://doi.org/10.1175/JAS-D-11-0251.1.

Raymond, D. J., 2000: Thermodynamic control of tropical rainfall. *Quart. J. Roy. Meteor. Soc.*, **126**, 889–898, https://doi.org/10.1002/qj.49712656406.

——, and X. Zeng, 2000: Instability and large-scale circulations in a two-column model of the tropical troposphere. *Quart. J. Roy. Meteor. Soc.*, **126**, 3117–3135, https://doi.org/10.1002/qj.49712657007.

Roach, W. T., 1976: On the effect of radiative exchange on the growth by the condensation of a cloud or fog droplet. *Quart. J. Roy. Meteor. Soc.*, **102**, 361–372, https://doi.org/10.1002/qj.49710243207.

Roberti, L., and C. Kummerow, 1999: Monte Carlo calculations of polarized microwave radiation emerging from cloud structures. *J. Geophys. Res.*, **104**, 2093–2104, https://doi.org/10.1029/1998JD200038.

Schlenczek, O., J. P. Fugal, G. Lloyd, K. N. Bower, T. W. Choularton, M. Flynn, J. Crosier, and S. Borrmann, 2017: Microphysical properties of ice crystal precipitation and surface-generated ice crystals in a high alpine environment in Switzerland. *J. Appl. Meteor.*, **56**, 433–453, https://doi.org/10.1175/JAMC-D-16-0060.1.

Schwartz, M. C., and G. G. Mace, 2010: Co-occurrence statistics of tropical tropopause layer cirrus with lower cloud layers as derived from CloudSat and CALIPSO data. *J. Geophys. Res.*, **115**, D20215, https://doi.org/10.1029/2009JD012778.

Shimizu, H., 1963: "Long prism" crystals observed in the precipitation in Antarctica. *J. Meteor. Soc. Japan*, **41**, 305–307, https://doi.org/10.2151/jmsj1923.41.5_305.

Shupe, M. D., and Coauthors, 2013: High and dry: New observations of tropospheric and cloud properties above the Greenland Ice Sheet. *Bull. Amer. Meteor. Soc.*, **94**, 169–186, https://doi.org/10.1175/BAMS-D-11-00249.1.

Skofronick-Jackson, G., and Coauthors, 2015: Global Precipitation Measurement Cold Season Precipitation Experiment (GCPEX): For measurement's sake, let it snow. *Bull. Amer. Meteor. Soc.*, **96**, 1719–1741, https://doi.org/10.1175/BAMS-D-13-00262.1.

——, A. Heymsfield, E. Holthaus, C. Albers, and M.-J. Kim, 2008: Nonspherical and spherical characterization of ice in Hurricane Erin for wideband passive microwave comparisons. *J. Geophys. Res.*, **113**, D06201, https://doi.org/10.1029/2007JD008866.

Slingo, A., and J. M. Slingo, 1988: The response of a general circulation model to cloud longwave radiative forcing. I: Introduction and initial experiments. *Quart. J. Roy. Meteor. Soc.*, **114**, 1027–1062, https://doi.org/10.1002/qj.49711448209.

Slingo, J. M., and A. Slingo, 1991: The response of a general circulation model to cloud longwave radiative forcing. II: Further studies. *Quart. J. Roy. Meteor. Soc.*, **117**, 333–364, https://doi.org/10.1002/qj.49711749805.

Small, J. D., and P. Y. Chuang, 2008: New observations of precipitation initiation in warm cumulus clouds. *J. Atmos. Sci.*, **65**, 2972–298, https://doi.org/10.1175/2008JAS2600.1.

Stephens, G. L., 1983: The influence of radiative transfer on the mass and heat budgets of ice crystals falling in the atmosphere. *J. Atmos. Sci.*, **40**, 1729–1739, https://doi.org/10.1175/1520-0469(1983)040<1729:TIORTO>2.0.CO;2.

——, S.-C. Tsay, P. W. Stackhouse, and P. J. Flatau, 1990: The relevance of the microphysical and radiative properties of cirrus clouds to climate and climatic feedback. *J. Atmos. Sci.*, **47**, 1742–1753, https://doi.org/10.1175/1520-0469(1990)047<1742:TROTMA>2.0.CO;2.

Stoelinga, M. T., J. D. Locatelli, and C. P. Woods, 2007: The occurrence of "irregular" ice particles in stratiform clouds. *J. Atmos. Sci.*, **64**, 2740–2750, https://doi.org/10.1175/JAS3962.1.

Takano, Y., and K. N. Liou, 1989: Solar radiative transfer in cirrus clouds. Part I: Single- scattering and optical properties of hexagonal ice crystals. *J. Atmos. Sci.*, **46**, 3–19, https://doi.org/10.1175/1520-0469(1989)046<0003:SRTICC>2.0.CO;2.

Tan, I., and T. Storelvmo, 2016: Sensitivity study on the influence of cloud microphysical parameters on mixed-phase cloud thermodynamic phase partitioning in CAM5. *J. Atmos. Sci.*, **73**, 709–728, https://doi.org/10.1175/JAS-D-15-0152.1.

Telford, J. W., 1996: Clouds with turbulence; the role of entrainment. *Atmos. Res.*, **40**, 261–282, https://doi.org/10.1016/0169-8095(95)00038-0.

Ulanowski, Z., E. Hirst, P. H. Kaye, and R. Greenaway, 2012: Retrieving the size of particles with rough and complex surfaces from two-dimensional scattering patterns. *J. Quant. Spectrosc. Radiat. Transfer*, **113**, 2457–2464, https://doi.org/10.1016/j.jqsrt.2012.06.019.

Voigtländer, J., and Coauthors, 2018: Surface roughness during depositional growth and sublimation of ice crystals. *Atmos. Chem. Phys.*, **18**, 13 687–13 702, https://doi.org/10.5194/acp-18-13687-2018.

Walden, V. P., S. G. Warren, and E. Tuttle, 2003: Atmospheric ice crystals over the Antarctic Plateau in winter. *J. Appl. Meteor.*, **42**, 1391–1405, https://doi.org/10.1175/1520-0450(2003)042<1391:AICOTA>2.0.CO;2.

Winker, D. M., and C. R. Trepte, 1998: Laminar cirrus observed near the tropical tropopause by LITE. *Geophys. Res. Lett.*, **25**, 3351–3354, https://doi.org/10.1029/98GL01292.

——, and Coauthors, 2010: The CALIPSO Mission: A global 3D view of aerosols and clouds. *Bull. Amer. Meteor. Soc.*, **91**, 1211–1229, https://doi.org/10.1175/2010BAMS3009.1.

Wu, T., W. R. Cotton, and W. Y. Y. Cheng, 2000: Radiative effects on the diffusional growth of ice particles in cirrus clouds. *J. Atmos. Sci.*, **57**, 2892–2904, https://doi.org/10.1175/1520-0469(2000)057<2892:REOTDG>2.0.CO;2.

Zeng, X., 2008: The influence of radiation on ice crystal spectrum in the upper troposphere. *Quart. J. Roy. Meteor. Soc.*, **134**, 609–620, https://doi.org/10.1002/qj.226.

——, 2018a: Radiatively induced precipitation formation in diamond dust. *J. Adv. Model. Earth Syst.*, **10**, 2300–2317, https://doi.org/10.1029/2018MS001382.

——, 2018b: Modeling the effect of radiation on warm rain initiation. *J. Geophys. Res. Atmos.*, **123**, 6896–6906, https://doi.org/10.1029/2018JD028354.

——, and Coauthors, 2007: Evaluating clouds in long-term cloud-resolving model simulations with observational data. *J. Atmos. Sci.*, **64**, 4153–4177, https://doi.org/10.1175/2007JAS2170.1.

——, and Coauthors, 2009: A contribution by ice nuclei to global warming. *Quart. J. Roy. Meteor. Soc.*, **135**, 1614–1629, https://doi.org/10.1002/qj.449.

——, W.-K. Tao, S. W. Powell, R. A. Houze Jr., P. Ciesielski, N. Guy, H. Pierce, and T. Matsui, 2013: A comparison of the water budgets between clouds from AMMA and TWP-ICE. *J. Atmos. Sci.*, **70**, 487–503, https://doi.org/10.1175/JAS-D-12-050.1.

——, G. Skofronick-Jackson, L. Tian, A. E. Emory, W. S. Olson, and R. A. Kroodsma, 2019: Analysis of the global microwave polarization data of clouds. *J. Climate*, **32**, 3–13, https://doi.org/10.1175/JCLI-D-18-0293.1.

——, J. Gong, X. Li, and D. L. Wu, 2021: Modeling the radiative effect on microphysics in cirrus clouds against satellite observations. *J. Geophys. Res. Atmos.*, **126**, e2020JD033923, https://doi.org/10.1029/2020JD033923.

Zhang, M., and Coauthors, 2001: Comparing clouds and their seasonal variations in 10 atmospheric general circulation models with satellite measurements. *J. Geophys. Res.*, **110**, D15S02, https://doi.org/10.1029/2004JD005021.

Zhou, C., P. Yang, A. E. Dessler, Y. Hu, and B. A. Baum, 2012: Study of horizontally oriented ice crystals with *CALIPSO* observations and comparison with Monte Carlo radiative transfer simulations. *J. Appl. Meteor. Climatol.*, **51**, 1426–1439, https://doi.org/10.1175/JAMC-D-11-0265.1.